



**HAL**  
open science

# Multi-annual and multi-decadal evolution of sediment accretion in a saltmarsh of the French Atlantic coast: Implications for carbon sequestration

B. Amann, E. Chaumillon, S. Schmidt, L. Olivier, J. Jupin, M.C. Perello, J.P. Walsh

## ► To cite this version:

B. Amann, E. Chaumillon, S. Schmidt, L. Olivier, J. Jupin, et al.. Multi-annual and multi-decadal evolution of sediment accretion in a saltmarsh of the French Atlantic coast: Implications for carbon sequestration. *Estuarine, Coastal and Shelf Science*, 2023, 293, pp.108467. 10.1016/j.ecss.2023.108467 . hal-04276241

**HAL Id: hal-04276241**

**<https://hal.science/hal-04276241>**

Submitted on 8 Dec 2023

**HAL** is a multi-disciplinary open access archive for the deposit and dissemination of scientific research documents, whether they are published or not. The documents may come from teaching and research institutions in France or abroad, or from public or private research centers.

L'archive ouverte pluridisciplinaire **HAL**, est destinée au dépôt et à la diffusion de documents scientifiques de niveau recherche, publiés ou non, émanant des établissements d'enseignement et de recherche français ou étrangers, des laboratoires publics ou privés.

1 **Multi-annual and multi-decadal evolution of sediment accretion in a saltmarsh of the French Atlantic**  
2 **coast: implications for carbon sequestration**

3

4 Amann, B.<sup>1</sup>, Chaumillon, E.<sup>1</sup>, Schmidt, S.<sup>2</sup>, Olivier, L.<sup>1</sup>, Jupin, J.<sup>3</sup>, Perello, M. C.<sup>2</sup>, Walsh, J. P.<sup>4</sup>

5 <sup>1</sup> *Littoral ENvironnement et Sociétés (LIENSs) - UMR 7266 CNRS, La Rochelle Université, 17000 La Rochelle, France*

6 <sup>2</sup> *Univ. Bordeaux, CNRS, Bordeaux INP, EPOC, UMR 5805, F-33600 Pessac, France*

7 <sup>3</sup> *Posgrado en Ciencias del Mar y Limnología, Universidad Nacional Autónoma de México. Av. Universidad 3000,*  
8 *Ciudad 6 Universitaria, Coyoacán, 04510 Ciudad de México, Mexico*

9 <sup>4</sup> *Coastal Resources Center, University of Rhode Island, Kingston, RI 02881, USA*

10

11

12 **Highlights**

- 13 • Saltmarshes prograde and aggrade at very high rates, keeping up with sea level rise  
14 • Sediment source proximity and accommodation space explain SAR spatial variability  
15 • Organic carbon accumulation rates are highly variable at the scale of a bay  
16 • Allochthonous C of marine origin prevails in long-term C sequestration

17

18

19 **Key words:** <sup>210</sup>Pb – LiDAR – organic carbon origin – Minerogenic saltmarsh – Blue Carbon – Nature-  
20 based solutions

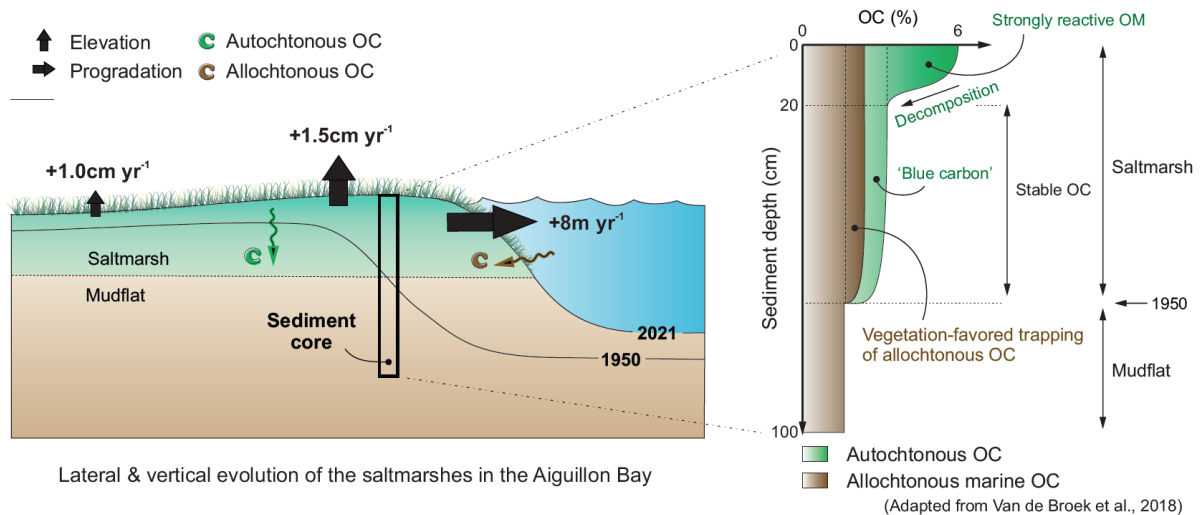
21 **Abstract**

22 Coastal marshes offer natural solutions for adapting to and mitigating the effects of climate change  
23 and sea level rise. However, the resilience of the marsh physical system and, with it, the ecosystem  
24 services that it provides, is largely site specific. This calls for the increase in the spatial cover of coastal  
25 marsh studies in order to assess the controlling factors of marsh evolution, and their long-term carbon  
26 storage capacities. Here, we study the spatio-temporal variations in sedimentation rates and organic  
27 carbon (OC) sequestration capacity of the macrotidal minerogenic saltmarshes in Aiguillon Bay,  
28 belonging to one of the largest French coastal marshes. Supported by aerial photographs and satellite  
29 image analysis, we first show that saltmarshes of the Aiguillon Bay have prograded at very high rates,  
30 up to 14 m yr<sup>-1</sup> since 1950. Sediment accumulation rates (SAR) were estimated at both multi-annual to  
31 multi-decadal scales based on two approaches: (i) LiDAR-based digital elevation models from multiple  
32 acquisition dates (2010-2021); and (ii) depth profiles of <sup>210</sup>Pb in excess and <sup>137</sup>Cs in sediment cores  
33 collected along cross-shore transects in the saltmarshes. Long-term SAR range from 0.8 to 2.2 cm yr<sup>-1</sup>  
34 and are among the highest reported worldwide for equivalent systems. The positive accretion balance  
35 (accretion rate minus local sea-level rise rate) provides important clues on marsh resilience suggesting  
36 that the Aiguillon Bay is currently able to adapt to rising sea level. Despite relatively low organic carbon  
37 content (1.3 to 6.0 %), high SAR leads to high carbon sequestration rates (99-345 gC m<sup>-2</sup> yr<sup>-1</sup>; or a mean  
38 value of 2.5 Mg C ha<sup>-1</sup> yr<sup>-1</sup>). The isotopic signature of sediment OC reveals a significant and rapid  
39 decomposition of organic material in surface cores, while allochthonous sediment of marine origin  
40 dominates the signature of chemically-stable OC of marsh sediments. This implies that the carbon  
41 sequestration capacity of minerogenic saltmarshes, such as those of the Pertuis Charentais, also  
42 depends upon the wealth of adjacent coastal environments through high sediment supply and primary  
43 productivity.

44

45 **Graphical Abstract**

46



47

48

49

50

## 51 1. Introduction

52 Saltmarshes offer natural solutions for adapting to and for mitigating the effects of global changes  
53 (Bertram et al., 2021; Costanza et al., 2014). Beyond many services such as ecological nurseries, tidal  
54 saltmarshes constitute a natural barrier against marine submersion, through their ability to  
55 accumulate sediment and to rise at the same time as the sea level, especially in macrotidal coastal  
56 areas (Crosby et al., 2016; Fagherazzi et al., 2020; Rogers et al., 2019). They protect the hinterland from  
57 flooding through their capacity to attenuate storm surges and waves, and they also offer natural  
58 solutions to buffer nutrient and pollutant inputs and to challenge the loss of biodiversity (Bij de Vaate  
59 et al., 2020; Leonardi et al., 2018). Saltmarshes are also critical environments for sediment organic  
60 carbon (OC) accumulation. Included in the 'blue carbon ecosystems' with mangroves and seagrass  
61 beds, saltmarshes contribute actively to the global carbon sink with burial rates of up to 15 Tg C yr<sup>-1</sup>  
62 (Lovelock and Reef, 2020; Macreadie et al., 2019). The blue-carbon function is increasingly recognized  
63 as an important lever for climate change mitigation, and for the implementation of nature-based  
64 solutions in particular (Hendriks et al., 2020; IPCC, 2022; Vinent et al., 2019).

65 The geomorphological evolution of saltmarshes largely controls the conservation of the ecosystem  
66 services they provide. The resilience of the marsh physical system and its biota is largely site specific  
67 and depends upon various conditions such as the tidal regime, the sediment supply, and the exposure  
68 to wind and waves (Fagherazzi et al., 2020). Saltmarshes are dynamic systems able to develop laterally,  
69 and to elevate their topography in response to sea level rise. Thus, fully understanding its horizontal  
70 and vertical dynamics is key to determining their fate in the next decades. This is particularly relevant  
71 for the OC sequestration potential (Lovelock and Reef, 2020).

72 Despite considerable scientific efforts, the number of saltmarsh studies remain under-represented  
73 compared to studies on mangroves and seagrass (e.g., 13% of valuation studies for blue carbon  
74 ecosystems concern saltmarshes, for the period 2007-2018; Himes-Cornell et al., 2018), and they do  
75 not yet warrant accurate upscaling of carbon sequestration rates at a continental or global scale  
76 (Macreadie et al., 2019). As an example, a single French study (Hensel et al., 1999) is considered in the  
77 first blue carbon review by Chmura et al., (2003), and resumed in subsequent ones (e.g., Duarte et al.,  
78 2005; Mcleod et al., 2011; Ouyang and Lee, 2014; Regnier et al., 2022). This calls for the increase in the  
79 spatial cover of coastal studies in order to evaluate the role of forcing parameters on marsh evolution,  
80 and on their long-term carbon sequestration and storage capacities (Ouyang and Lee, 2022). Also,  
81 while carbon stocks (e.g., in Mg C ha<sup>-1</sup>) are generally well identified, carbon accumulation rates from  
82 coastal habitats are rarely addressed (in Mg C ha<sup>-1</sup> yr<sup>-1</sup>; Arias-Ortiz et al., 2018; Jennerjahn, 2020).  
83 Recent reviews on blue carbon research also stressed the need to improve our understanding of the  
84 source and stability of OC in saltmarshes (Macreadie et al., 2019; Windham-Myers et al., 2019).

85 In this context, the French Atlantic coast offers a good opportunity to contribute to the global  
86 catalogue of saltmarsh studies by documenting sediment and carbon accumulation rates from  
87 macrotidal systems. Here we study saltmarshes of the Aiguillon Bay; a highly dynamic system that is  
88 connected to small rivers. Seaward shoreline migration was shown at both long- and medium-time  
89 scales, respectively with rates of 70 km over the last 2000 years (Chaumillon et al., 2004) and up to  
90 7 ha an<sup>-1</sup> during the last 50 years (Godet et al., 2015). This suggests that the Aiguillon Bay potentially  
91 accumulates a large amount of sediment and maintains an efficient carbon sequestration capacity.

92 With this in mind, our study aims at: (i) understanding the morphological evolution of saltmarshes; and  
93 (ii) quantifying the long-term carbon sequestration capacity of these coastal wetlands. First, we build  
94 up a picture of the lateral and vertical evolution of the Aiguillon marshes at the multi-annual and multi-  
95 decadal time scales. For this, we combine the reconstruction of the saltmarsh boundary through aerial  
96 and satellite imagery analysis, with sediment accumulation rates derived by two methods: (i) <sup>210</sup>Pb-

97 derived dating of sediment cores collected along two cross-shore transects; and supported by (ii)  
98 LiDAR-based digital elevation models from multiple acquisition dates. Then, we discuss the origin and  
99 fate of organic material (OM) preserved in coastal environments using elemental OC content, C/N,  
100  $\delta^{13}\text{C}$ , and  $\delta^{15}\text{N}$  from landward and seaward locations. Finally, we discuss the rapid accumulation of  
101 sediment and the relatively high carbon sequestration capacity of the studied saltmarshes, with  
102 respect to the international literature. Our results may provide a decision support tool for the  
103 implementation of nature-based solutions in coastal management strategies (e.g., Dupuy et al., 2022).

104

## 105 **2. Study site**

106 The Aiguillon Bay is located on the southwestern Atlantic French coast, which opens onto the Pertuis  
107 Breton between Ré Island and the Vendée Coast (Fig. 1). The Pertuis Breton forms a major embayment  
108 opened to the Atlantic Ocean that corresponds to the drowned incised valley segment of the Lay, Sèvre  
109 Niortaise, and Vendée Rivers (Chaumillon et al., 2008).

110 The Aiguillon Bay is a cove, semi-enclosed by the so-called “Pointe de l'Aiguillon”, a sand spit  
111 developing from the northwest to the southeast (Fig. 1). It is characterized by lowland coastal  
112 environments, which include one of the largest coastal marshes of France (1100 ha) fronted by  
113 extensive tidal flats (3700 ha). The cove receives freshwater and a part of the fine sediments from the  
114 Sèvre Niortaise ( $12 \text{ m}^3 \text{ s}^{-1}$ ) and the Lay rivers ( $2 \text{ m}^3 \text{ s}^{-1}$ ) predominantly (Banque HYDRO, 1969/2017),  
115 and from several smaller channels secondarily (Coignot et al., 2020; Fig. 1). This region of the French  
116 coast is characterized by relatively high suspended sediment concentrations with  $4.0 \pm 3.1 \text{ mg L}^{-1}$   
117 reported locally (SOMLIT station, Pertuis Antioche; period 04.2020 – 03.2022; [www.somlit.fr](http://www.somlit.fr)).  
118 However, the fine sediment supply to the Aiguillon Bay is not well understood. Erosion of coastal  
119 Mesozoic limestones and marls outcrops may provide significant quantities of clay particles to the bay.  
120 It cannot be excluded that fine sediments are also supplied by the Gironde Estuary, whose sediment  
121 input to coastal waters was estimated to  $1.6 \text{ Mt yr}^{-1}$  (Doxaran et al., 2009;  
122 Schmitt and Chaumillon, 2023). The dispersion of the estuarine plume of the Gironde could reach the  
123 Marennes-Oléron Bay located 45 km in the south of the Aiguillon Bay (Constantin et al., 2018; Poirier  
124 et al., 2016).

125 The area is characterized by a semi-diurnal macrotidal regime with mean tidal range of c. 4 meters and  
126 strong tidal currents (Dodet et al., 2019). This part of the French coastline is characterized by low-lying  
127 coastal zones particularly vulnerable to flooding (Baumann et al., 2017; Bertin et al., 2014; Breilh et al.,  
128 2014, 2013). The studied area has experienced six major marine floods over the 20<sup>th</sup> and 21<sup>st</sup> centuries  
129 (Breilh et al., 2014). The last major marine flood was caused by the storm Xynthia (28/02/2010), which  
130 induced an exceptional storm surge (1.6 m in La Rochelle Harbor) in phase with high spring tide  
131 resulting in extensive flooding of low-lying coastal zones (Bertin et al., 2012; Breilh et al., 2013).

132 The Aiguillon Bay bears witness to the successive land reclamation history of the Marais Poitevin, which  
133 have gradually reduced the ancient Gulf of Pictons (Godet et al., 2015; Godet and Thomas, 2013;  
134 Verger, 2009; Fig. 1a). Today, the bay includes 1100 ha of saltmarshes among which about half is  
135 subject to mowing (Fig. 1c, d). The halophytic vegetation is dominated by C3 plants such as marine  
136 *Puccinellia* (*puccinellia maritima*) and Sea Purslane (*halimione portulacoides*). C4 plants are also  
137 present, with *Agropyron* (*agropyron pungentis*) that commonly develop in topographic high, while  
138 Marine *Spartina* (*Spartina maritima*) and a few annual *Salicornia* (*Salicornia sp*) compose lowland areas  
139 of the saltmarsh (Fig. S1). The Aiguillon Bay has been fully classified as a National Nature Reserve in  
140 1999 for its fauna and ornithological richness.

### 141 3. Materials and methods

#### 142 3.1. Aerial & satellite imagery

143 Aerial photographs and satellite images were used to reconstruct the lateral evolution of the saltmarsh  
144 boundary (boundary between the mudflat and the saltmarsh) in the Aiguillon Bay, from 1950 to 2020.  
145 Digitized aerial photographs from 1950 to 2010 (source: *IGN, France*) were mosaicked, georeferenced  
146 and ortho-rectified using Geomatica v.9<sup>®</sup> software. The mapping of the bay did not integrate marshes  
147 located in the meander of the Sèvre Niortaise. Roads and parking areas around the bay were used as  
148 control points for the geo-referencing. The most recent evolutions of the saltmarshes were derived  
149 using the SPOT-6 Satellite Image Gallery, for the years 2015-2020. The spatial uncertainty (SU) was  
150 estimated following (Ford, 2012):

$$151 \quad SU = \sqrt{PU^2 + GU^2 + DU^2} \quad (\text{in m})$$

152 where PU, GU and DU are the pixel size, Geo-referencing, and Digitizing Uncertainties, respectively. PU  
153 and GU were derived from the metadata of the source images (Table S1), while DU was estimated from  
154 digitizing replicates of aerial photographs and orthophotos.

155 The rate of progression of the saltmarsh boundary (in m yr<sup>-1</sup>) was calculated for the period 1950-2020  
156 using the USGS DSAS v5 tool (Himmelstoss et al., 2018). For this, a baseline was generated from a  
157 buffer zone of 100 m around the combined vegetation lines of 1950, and the seaward part of the buffer  
158 zone was defined using the tracing tool from the 2020 imagery. Cross-shore transects were defined in  
159 this way, every 50 m covering the entire bay. A mean SU of 8.8 m was implemented into the DSAS v5  
160 calculations, for the period 1950-2020. A tolerance of 20 m and a smoothing of 1000 were assigned.

#### 161 3.2. Sediment coring and processing

##### 162 3.2.1. Sediment coring

163 Five sediment cores were collected from two cross-shore transects of the Aiguillon Bay saltmarshes,  
164 using a Russian corer; one core was collected in July 2017, and four in June 2021 (Fig. 1). The coring  
165 sites were selected to meet the following criteria: (i) they are placed on the saltmarsh boundary  
166 mapped for a given year, thus allowing to constrain the age of the transition between a pre-existing  
167 mudflat environment and the saltmarsh; (ii) they are representative of the ecosystem of the bay  
168 covering landward, seaward and intermediate zones of the saltmarsh; and (iii) the targeted marsh soil  
169 profiles develop under the same management type over the decades, namely free of mowing activity,  
170 thus focusing on the 'natural' evolution of the saltmarshes of the bay. Three 1.1-m long cores were  
171 thus collected along a cross-shore transect from the northern bay (AIG21\_20, AIG21\_21, and  
172 AIG21\_22; Fig. 1b). AIG21\_22 was retrieved from the high marsh dominated by a C4-plant environment  
173 (*Marine Puccinellia*, and Sea Purslane), hereafter mentioned as the landward site. AIG21\_20 was  
174 retrieved from the low marsh close to the ocean characterized by the presence of C3 and C4 plants  
175 (e.g., *Marine Spartina*), hereafter mentioned as the seaward site. AIG21\_21 corresponds to the  
176 intermediate location. Two short cores (length < 50 cm) were collected from saltmarshes located at  
177 the mouth of the Sèvre Niortaise River in order to assess the influence of river proximity on  
178 sedimentation rates and carbon accumulation potential (AIG21\_11, AIG17\_01; Fig. 1c; Fig. S2).

179 3.2.2. Dry bulk density

180 Each 2021 core was sectioned at a 1cm resolution, and samples were freeze-dried for 72 h to  
181 determine the water content, the dry bulk density (DBD), and radionuclides of interest. The 2017 core  
182 was only sampled every 4 cm. All samples were ground gently using a mortar for further analyses.

183 3.2.3. Organic matter content, TOC, TN,  $\delta^{13}\text{C}$  and  $\delta^{15}\text{N}$

184 High-resolution (every 1 cm) and cost-effective profiles of organic matter (OM) content were first  
185 obtained using loss on ignition (LOI) to constrain the sample selection for elemental and isotope  
186 analyses of carbon and nitrogen. The LOI analysis was performed at a temperature of combustion of  
187 550°C for 14 h (Baustian et al., 2017; Wilson and Allison, 2008). Due to the diversity of temperatures  
188 and durations used for LOI in the literature, the protocol with the lowest reported temperature of  
189 combustion (450°C for 8 h) was also tested for comparison (Craft et al., 1991; Howard et al., 2014;  
190 Fig S3). We used an elemental analyzer (EA Isolink, Thermo Scientific) to measure organic carbon and  
191 total nitrogen contents from selected samples in each core.

192 Total organic carbon (TOC), total nitrogen (TN), and  $\delta^{13}\text{C}$  and  $\delta^{15}\text{N}$  isotopes were determined on the  
193 2021 sediments using an EA-IRMS at the LIENSs Stable Isotope Facility, La Rochelle University, France  
194 (EA Isolink, Thermo Scientific; Delta V Plus with a Conflo IV interface, Thermo Scientific). The analyses  
195 were duplicated on samples after acidification for TOC and  $\delta^{13}\text{C}$ , and on raw samples for  $\delta^{15}\text{N}$  to  
196 prevent the effects of acidification on  $\delta^{15}\text{N}$  values (Lebreton et al., 2011). A correction factor was  
197 applied to the TOC measurements using total nitrogen as a proxy for the changing weight induced by  
198 sample acidification. 100 mg of dry sediment were acidified with 0.5N HCl to remove the carbonates,  
199 and dried overnight in a dry bath at 60°C under N<sub>2</sub> filtered airflow. 1 mL MilliQ water was then added  
200 to the sample, which was freeze-dried and grounded again. An optimal weight of 5 mg of sediment  
201 was added to 8 x 5 mm tin capsules for analysis. Isotopic values were expressed in the  $\delta$  unit notation  
202 as deviations from standards (Vienna Pee Dee Belemnite for  $\delta^{13}\text{C}$  and atmospheric N<sub>2</sub> for  $\delta^{15}\text{N}$ )  
203 following the formula:

204 
$$\delta^{13}\text{C} \text{ or } \delta^{15}\text{N} = \left( \frac{R_{\text{sample}}}{R_{\text{standard}}} - 1 \right) \cdot 10^3, \text{ where R is } ^{13}\text{C}/^{12}\text{C} \text{ or } ^{15}\text{N}/^{14}\text{N}, \text{ respectively}$$

205 Reference materials USGS-61 and USGS-63 (Caffeine) were used for calibration and for uncertainty  
206 calculation. Standard deviations were 0.11 % for carbon, 0.10 % for nitrogen, and 0.05 ‰ for  $\delta^{13}\text{C}$  and  
207 0.04 ‰ for  $\delta^{15}\text{N}$ .

208 The TOC content measured by elemental analysis was used to calculate organic carbon accumulation  
209 rates in each sediment core. Sediment  $\delta^{13}\text{C}$  and  $\delta^{15}\text{N}$  combined with C/N ratios were used to assess  
210 the origin of OC; namely to distinguish between an autochthonous and an allochthonous source.  
211 Below-ground biomass (BGB) was separated from the bulk sediment in top cores and also analyzed by  
212 EA-IRMS following the same protocol as for the bulk sediment.

213 3.2.4. Sediment grain size

214 Grain-size analysis was performed every three samples using a Malvern Mastersizer 2000 laser particle  
215 size analyzer at EPOC (France). Sample selection followed those of the sampling strategy for dating in  
216 order to assess a potential effect of changing grain size on the age-depth modeling. Prior to analysis,  
217 the terrigenous fraction was isolated by removing organic matter, calcium carbonate, and biogenic  
218 silica through H<sub>2</sub>O<sub>2</sub> (35%), HCl (10 to 50%), and NaOH (1N) chemical pre-treatments, respectively. Due  
219 to the high organic matter content, this pre-treatment and grain size analysis were performed after  
220 combustion of the sediment samples for 14h at 550°C. Adjustment of the material optical properties  
221 was needed in order to reduce the weighted residuals induced by the red color of these pre-combusted  
222 materials. For this, the refractive and absorption index of red pigments were selected from the optical

223 property analyzer tool of the Malvern 2000 software (RI = 2.52, AI = 0.1, respectively). This ensured an  
224 optimal fit between measured and modeled grain size data. Finally, a solution of sodium  
225 hexametaphosphate (NaPO<sub>3</sub>, 2%) was used to prevent clay flocculation before analysis. Grain-size  
226 distribution averages were obtained from three replicates, each measured for 12 s after 10%  
227 sonication.

### 228 3.2.5. Sediment, mass and organic carbon accumulation rates

229 Sediment accumulation rates (SAR, in cm yr<sup>-1</sup>) and mass accumulation rates (MAR, in g cm<sup>-2</sup> yr<sup>-1</sup>) at the  
230 multi-decadal scale were obtained using <sup>210</sup>Pb-based dating of the cores. <sup>210</sup>Pb (T<sub>1/2</sub> = 22.3 years) is a  
231 naturally-occurring radionuclide delivered continuously on Earth surface by atmospheric fallout and  
232 readily scavenged by particulate matter. This atmospherically derived <sup>210</sup>Pb is referred to as <sup>210</sup>Pb in  
233 excess (<sup>210</sup>Pb<sub>xs</sub>) of that supported in sediment derived from the *in situ* radioactive decay series of <sup>238</sup>U  
234 (Iurian et al., 2021, and references herein). The <sup>210</sup>Pb-based SAR were independently checked by the  
235 artificial radionuclide <sup>137</sup>Cs (T<sub>1/2</sub> = 30 years), which presents a maximum atmospheric fallout related to  
236 weapon tests in 1963.

237 For the cores collected in 2021, the activities of the radioelements of interest (<sup>210</sup>Pb, <sup>226</sup>Ra, <sup>232</sup>Th, <sup>137</sup>Cs)  
238 were measured using a high-efficiency, low-background broad energy gamma detector equipped with  
239 a Cryo-Cycle II (Mirion) at EPOC, University of Bordeaux (Dubosq et al., 2021). <sup>226</sup>Ra was determined  
240 using selected gamma rays emitted by its short-lived decay products (<sup>214</sup>Pb and <sup>214</sup>Bi), implying that  
241 measurements were performed at least 3 weeks after 6-8 g aliquots of dry sediment were placed in  
242 the counting vials to ensure equilibrium. <sup>210</sup>Pb, <sup>232</sup>Th and <sup>137</sup>Cs were determined by their gamma ray at  
243 46.5, 238 and 662 keV, respectively (Reyss et al, 1995). Calibration of the detector was obtained using  
244 certified reference material (IAEA-RGU-1; SOIL-6). For AIG17\_01, <sup>210</sup>Pb was measured by alpha  
245 spectrometry following the methodology described in Corbett and Walsh (2015). Activities are  
246 expressed in mBq g<sup>-1</sup> and errors calculated using 1-standard deviation counting statistics. Excess <sup>210</sup>Pb  
247 was calculated by subtracting the measured <sup>226</sup>Ra from the total measured <sup>210</sup>Pb activity. <sup>210</sup>Pb was  
248 normalized considering <sup>232</sup>Th in order to reduce the impact of changes in sediment composition (Stupar  
249 et al., 2014), due to a variable proportion of vegetal fraction in saltmarsh sediments. Sediment and  
250 mass accumulation rates were determined from the slope of the <sup>210</sup>Pb<sub>xs</sub><sup>Th</sup> profiles against depth and  
251 cumulative mass, using the CF:CS model (constant flux and constant sedimentation). For AIG17-01,  
252 calculations were done on <sup>210</sup>Pb<sub>xs</sub> in the absence of <sup>232</sup>Th determination. The mudflat/marsh transition  
253 in the core was determined by matching information based on: (i) marsh vegetation boundaries  
254 mapped at different years from aerial photos and satellite images, (ii) <sup>210</sup>Pb dating of the sediments  
255 downcore, and (iii) changes in the isotopic signature of the sedimentary organic matter.

256 Organic carbon accumulation rates (CAR, in g cm<sup>-2</sup> yr<sup>-1</sup>) were calculated as the product of the mean  
257 sediment OC content (in %), and mass accumulation rates based on the <sup>210</sup>Pb<sub>xs</sub><sup>Th</sup> profiles of the  
258 sediment cores (in g cm<sup>-2</sup> yr<sup>-1</sup>). The sections of the OC and δ<sup>13</sup>C profiles reaching a rather constant and  
259 minimum value in depth (< 2\*standard deviation) were interpreted as the effectively-preserved OC  
260 stocks, thus representing the long-term carbon sequestration capacity of the saltmarsh. In topsoil  
261 sediments, labile autochthonous OC inputs can control short-term OC deposition rates (Mueller et al.,  
262 2019; Van de Broek et al., 2018). Thus, the upper section of each core was excluded from the CAR  
263 calculation to avoid an overestimation of the long-term OC sequestration rates (expressed in Mg C ha<sup>-1</sup>  
264 yr<sup>-1</sup>).

265

### 266 3.3. LiDAR data



267 Saltmarsh accumulation rates at the multi-annual scale were obtained from LiDAR-derived digital  
268 elevation models (DEMs) obtained from 2010 to 2021. SAR estimates from LiDAR data are used to  
269 support the orders of magnitude in SAR obtained at the multi-decadal scale by sediment core analysis.  
270 LiDAR is a generalized remote-sensing method used to gauge the evolutions at the earth's surface. By  
271 measuring the reflected light that bounces off the ground and back to the sensor fixed on a plane, it  
272 provides accurate mapping of surface elevation from coastal environments (Collin et al., 2010;  
273 Medeiros et al., 2022). Differences between DEMs obtained during successive years were used to map  
274 surface elevation changes and to assess short-term sediment accumulation rates in the Aiguillon  
275 saltmarshes.

276 The most recent LiDAR data were acquired for the entire bay in September 2016 and October 2021  
277 (*OPSIA Company, Toulon*). Data were collected using a laser scanner RIEGL VQ-780 II mounted on a  
278 Partenavia P68 Observer2 from an altitude of 750 m and 1650 m in 2016 and 2021, respectively. It  
279 provided a gaining density of 10 points/m<sup>2</sup>. The vertical accuracy was derived from twenty ground-  
280 control points (GCPs) using a RTK-GPS on roads and parking around the bay. The root mean squared  
281 error for the height difference between LiDAR and RTK-GPS data was 2.5 and 3.4 cm for 2016 and 2021,  
282 respectively (Table S1). Previous LiDAR data were collected in July 2010, and in February 2013. These  
283 data were acquired with a point density of 3 points/m<sup>2</sup> using a laser scanner RIEGL VQ-820-G in 2010  
284 (*Institut Géographique National IGN, France*), and using a laser scanner RIEGL LiteMapper-6800 in 2013  
285 (*Aerodata Company, Marçq-en-Baroeul, France*). 376 GCPs were defined, and the vertical accuracy was  
286 calculated by comparing LiDAR data of 2010 and 2013, with the reference LiDAR data of 2016. This  
287 resulted in a vertical accuracy of 7 and 2 cm for 2010 and 2013, respectively (Table S2).

288 Differences in LiDAR-based DEMs were used to assess short-term (decadal) sediment accumulation  
289 rates by estimating the volume of sediment accumulated over saltmarshes of the whole bay, through  
290 time (in m<sup>3</sup>). These estimates accounted for marsh-elevation changes and for the progradation of the  
291 saltmarsh boundary between two periods of acquisition. The sediment volume in the salt marsh was  
292 then divided by the salt-marsh area to calculate mean sediment accumulation rates over different  
293 periods (2010-2021, 2013-2021, and 2016-2021; Table 2). Sediment accumulation rates for the entire  
294 instrumental period 2010 to 2021 were used to support orders of magnitude in accumulation rates  
295 derived from <sup>210</sup>Pb-derived dating of sediment cores. This integration of LiDAR data over 11 years has  
296 the advantage of reducing uncertainties associated with the vertical accuracy of each annual DEM.  
297 Contrary to sediment core data, LiDAR data covers the entire bay that allows us discussing the spatial  
298 and temporal variability of saltmarsh accretion over the last 20 years. Because TOC measurements are  
299 bound to the multi-decadal time scale, LiDAR data was not used to calculate carbon accumulation rates  
300 at the multi-annual time scale.

301

## 302 4. Results

### 303 4.1. Lateral evolution of the saltmarshes

304 The reconstruction of the saltmarsh boundary using aerial photographs and satellite images shows a  
305 global progradation toward the ocean since 1950 (Fig. 2). Data disclose a mean gradual seaward  
306 migration of  $8 \text{ m yr}^{-1}$  for the whole bay, and a maximum of  $14 \text{ m yr}^{-1}$  for the northern bay (Fig. 2a). This  
307 corresponds to a mean net gain in saltmarsh area of  $8 \text{ ha yr}^{-1}$  (Fig. 2b). The most recent land  
308 reclamations date back to 1963 and 1965, and are located in the southeastern and the northwestern  
309 bay, respectively. These land claims induced a reduction of 200 ha in the saltmarsh area, from 1960 to  
310 1972 (Fig. 2b). The saltmarsh has gained surface at relatively constant pace throughout the last two  
311 decades. The greatest progradation is in the northern bay, close to the Chenal Vieux and between  
312 vegetated tips that develop all around the bay (Fig. 2a).

### 313 4.2. Sediment composition

314 Sediments of the Aiguillon bay are composed predominantly of fine silt and clay at  $81 \pm 5 \%$  and  
315  $17 \pm 5 \%$  respectively, with mean grain size of  $6.7 \pm 1.6 \mu\text{m}$  (Fig. 3). OM content ranges from 12 to 24 %,  
316 and OC content from 1.1 to 6.1 % (Fig. S3), with the highest values found in the top of the sediment  
317 cores. These rather low OC levels categorize the saltmarshes of the Aiguillon Bay as minerogenic  
318 marshes; i.e., marshes that are dominated by mineral sediment input supplied by the inundating  
319 water.

320 Along the northern transect, AIG21\_22 core presents a clear change at 20 cm depth. OM and OC  
321 content are maximal at the surface of the core until 7.5 cm, with a mean OC value of 4.5 % (Fig. 3). This  
322 value quickly drops to 2.7 % until 20 cm, and then reaches a minimum and relatively stable value of  
323  $1.4 \pm 0.1 \%$  until the base of the core. Maximum OC values are also found at the surface of the cores  
324 of AIG21\_21 and AIG21\_20 with 3.7 % and 3.5 %, respectively. These values decrease significantly with  
325 depth and stabilize below 20 cm in both cores, with mean OC of  $1.7 \pm 0.2 \%$  and  $2.3 \pm 0.2 \%$  for  
326 AIG21\_20 and AIG21\_21, respectively.

327 The three cores contrast by their carbon and nitrogen isotopic profiles.  $\delta^{13}\text{C}$  is minimal at the surface  
328 of cores AIG21\_22 and AIG21\_21 with mean values of  $-26.4 \text{ ‰}$  and  $-23.6 \text{ ‰}$ , respectively. This value  
329 increases downcore reaching a mean of  $-22.0 \text{ ‰}$  for AIG21\_22 and  $-18.1 \text{ ‰}$  in AIG21\_21, towards the  
330 base of the cores. The  $\delta^{13}\text{C}$  profile of the seaward site AIG21\_20 presents an opposite pattern with  
331 maxima found at the surface averaging  $-16.9 \text{ ‰}$ , and a mean of  $-21.9 \text{ ‰}$  found towards the base.  $\delta^{15}\text{N}$   
332 gradually decreases with depth in all cores. This trend is more pronounced in AIG21\_22 with a surface  
333 value of  $9.4 \text{ ‰}$  and a minimum of  $6.9 \text{ ‰}$  found at the base of the core. AIG21\_21 shows a decrease  
334 from  $8.7 \text{ ‰}$  to  $7.0 \text{ ‰}$ , and AIG21\_20 from  $7.7 \text{ ‰}$  to  $7.3 \text{ ‰}$ .

335 Along the eastern transect, the short core AIG21\_11 show profiles of OC and  $\delta^{13}\text{C}$  similar to that of the  
336 landward site AIG21\_22 (Fig. S2). OC content decreases from 6.1 % at the surface to 1.5 % at the core  
337 basal.  $\delta^{13}\text{C}$  is enriched from surface to base, with mean values ranging from  $-26.6 \text{ ‰}$  to  $-19.6 \text{ ‰}$ .

338 Grain size does not differ significantly between cores and between samples within each core, with  
339 geometric mean grain size of  $7.6 \mu\text{m}$  for AIG21\_22,  $6.4 \mu\text{m}$  for AIG21\_21, and  $6.2 \mu\text{m}$  for AIG21\_20.  
340 This suggests that bulk sediment material accumulated in saltmarshes of the Aiguillon Bay is  
341 unchanged through time and between locations.

### 342 4.3. Vertical evolution of the saltmarshes

#### 343 4.3.1. Sediment and mass accumulation rates

344  $^{210}\text{Pb}_{\text{xs}}$  activities are quite similar in surface sediment of all the cores (c. 100 mBq g<sup>-1</sup>), and decrease  
345 exponentially with sediment depth (Fig. 4). In contrast, the maximum penetration depth of  $^{210}\text{Pb}_{\text{xs}}$  is  
346 extremely variable among the cores. While negligible excesses are reached at about 80 cm in core  
347 AIG21\_22,  $^{210}\text{Pb}_{\text{xs}}$  activities are only half the surface values at 100 cm in core AIG21\_20. Even if such  
348 penetrations correspond to significant sedimentary accumulation, this suggests large disparities in the  
349 rate of sedimentation between the different sites. The decrease in  $^{210}\text{Pb}_{\text{xs}}$  present some irregularities  
350 as observed from 40 to 43 cm on core AIG21\_22 with lower excesses compared to the surrounding  
351 layers. Assuming that this layer corresponds to a specific event (relocation of older sediment), the  
352 evidence of this event was actively suppressed from the profile to produce an event-free  $^{210}\text{Pb}_{\text{xs}}^{\text{Th}}$   
353 profile on which a mean SAR was calculated. This allows comparing long-term SAR estimates between  
354 the different cores in the Aiguillon saltmarshes.  $^{232}\text{Th}$  activities range between 28 to 55 mBq g<sup>-1</sup>, with  
355 the lowest values measured in the upper sections. Surface sediments also present the highest total  
356 carbon content resulting in a dilution of the detrital fraction as traced by the long-lived  $^{232}\text{Th}$  ( $T_{1/2} = 14$   
357  $10^9$  years). This dilution effect also has an impact on  $^{210}\text{Pb}$  as shown by the comparison of surface  $^{210}\text{Pb}_{\text{xs}}$   
358 and  $^{210}\text{Pb}_{\text{xs}}^{\text{Th}}$  activities (Fig. 4). Th-corrected  $^{210}\text{Pb}_{\text{xs}}$  is thus preferred to avoid overestimating sediment  
359 accumulation rates.

360 The depth of the  $^{137}\text{Cs}$  peak corresponding to the year 1963 was also used to test the robustness of the  
361 sediment and mass accumulation rates derived from the  $^{210}\text{Pb}_{\text{xs}}^{\text{Th}}$  profiles.  $^{137}\text{Cs}$  activities are low  
362 (< 10 mBq g<sup>-1</sup>) in all profiles, except for a peak in core AIG-21\_22 and to a lesser extent in core  
363 AIG21\_21. In AIG21\_22, a clear  $^{137}\text{Cs}$  peak is found at 51 cm that lies within the error range of the  $^{210}\text{Pb}$   
364 model that estimates a depth of  $49 \pm 3$  cm for this chronomarker. Similarly in AIG21\_21,  $^{137}\text{Cs}$  activity  
365 peaks at 106.5 cm, expected at  $107 \pm 5$  cm using the  $^{210}\text{Pb}$  model. The high sedimentation rates of  
366 AIG21\_20, as derived from the  $^{210}\text{Pb}$  model ( $2.2 \pm 0.3$  cm yr<sup>-1</sup>), does not allow pointing at the year 1963  
367 for the 110-cm long sequence (projected depth of  $129 \pm 19$  cm). The  $^{137}\text{Cs}$  profile of AIG21\_20 thus  
368 shows a gradual increase with depth.

369  $^{210}\text{Pb}_{\text{xs}}^{\text{Th}}$  profiles result in high mean apparent sedimentation accumulation rates (SAR) ranging from  
370 0.84 to 2.22 cm yr<sup>-1</sup>, with corresponding mass accumulation rates (MAR) of 0.74 to 1.83 g cm<sup>-2</sup> yr<sup>-1</sup>  
371 (Table 1). On the northern transect, the lowest sedimentation rates are found for the landward site  
372 (AIG21\_22), while the highest values are found for the seaward site (AIG21\_20). Short cores located  
373 close to the river mouth (AIG21\_11, and AIG17\_01) have intermediate values of 1.24 cm yr<sup>-1</sup> and 1.41  
374 cm yr<sup>-1</sup> (0.86 and 1.24 g cm<sup>-2</sup> yr<sup>-1</sup>), respectively.

#### 375 4.3.2. Spatial and temporal variability of saltmarsh accretion using LiDAR data

376 LiDAR data demonstrate that the saltmarshes of the Aiguillon Bay have rapidly accumulated sediment  
377 over the last decade. A net sediment gain of  $1\,419\,043 \pm 458\,732$  m<sup>3</sup> was found between 2010 and  
378 2021, which corresponds to a mean sedimentation rate of  $1.17 \pm 0.38$  cm yr<sup>-1</sup> for a surface area of  
379  $1\,100\,000$  m<sup>2</sup> in 2021 (Table 2, Fig. 5a). Mean sedimentation rates progressively decrease through time  
380 with  $0.48 \pm 0.24$  cm yr<sup>-1</sup> for the period 2013-2021, and  $0.39 \pm 0.49$  cm yr<sup>-1</sup> for 2016-2021 (Table 2).  
381 LiDAR results also show an important spatial heterogeneity in marsh vertical evolution. Maximum  
382 vertical gains are found at the saltmarsh boundary and at the foot of the dikes, with values > +1.0 m  
383 for the period from 2010 to 2021. High sediment accumulation > +0.8 m also characterizes areas  
384 located close and along the channels (Fig 5a). In contrast, minimum gains below 0.1 m are found  
385 landward, and from the zones characterized by mowing activity in the northern bay.

386 LiDAR-based SAR estimates for the entire instrumental period are consistent with sediment-core data  
387 at the coring sites, except for the site cored in 2017 (Fig 5b). Data show an increasing trend along the  
388 cross-shore transect from shoreward to seaward coring locations. Reported LiDAR values for the coring  
389 locations of the northern transect AIG21\_22, 21, and 20 are 1.2, 2.2, and 2.9 cm yr<sup>-1</sup>, respectively for  
390 the period 2010-2021. LiDAR values for the coring locations of the eastern transect AIG21\_11, and  
391 AIG17\_01 are 2.2, and 3.2 cm yr<sup>-1</sup>, respectively. These values were derived using a 3 x 3 m grid around  
392 the coring sites to account for spatial variability and for the GPS uncertainty in locating the coring sites.

#### 393 **4.4. Organic carbon accumulation rates**

394 Along the north transect, organic carbon accumulation rates (CAR) are marked by a great  
395 heterogeneity among the cores, reflecting varying rates of carbon deposition in different locations  
396 (Table 1). The landward location (AIG21\_22) displays the lowest CAR value of  $107 \pm 11 \text{ g cm}^{-2} \text{ yr}^{-1}$ ,  
397 suggesting a relatively slower rate of organic carbon accumulation. In contrast, the intermediate  
398 location (AIG21\_21) and the seaward location (AIG21\_20) exhibit higher CAR values of  
399  $373 \pm 5 \text{ g cm}^{-2} \text{ yr}^{-1}$  and  $340 \pm 29 \text{ g cm}^{-2} \text{ yr}^{-1}$ , respectively, indicating more rapid organic carbon  
400 deposition in these areas. The site closer to the river mouth (AIG21\_11) displayed an intermediate CAR  
401 value of  $182 \pm 48 \text{ g cm}^{-2} \text{ yr}^{-1}$  (Table 1). The heterogeneity in CAR values among the cores emphasizes  
402 the complexity of carbon dynamics in saltmarsh environments and highlights the need for site-specific  
403 investigations to understand the underlying processes governing sediment and carbon accumulation.

404 To estimate these CAR values, we used the organic carbon (OC) content measured by an elemental  
405 analyzer, ensuring that the results represented the true OC content in the sediment. We conducted  
406 multiple tests using different combustion durations and temperatures to verify the accuracy of the LOI  
407 (Loss on Ignition) technique for determining total organic carbon (TOC) percentages (Fig. S3). Our  
408 findings revealed that the LOI technique alone cannot be used for a quantitative determination of TOC  
409 percentages. As a result, we relied on the elemental analyzer to accurately assess the OC content and  
410 subsequently calculate the organic carbon accumulation rates.

## 411 5. Discussion

### 412 5.1. The Aiguillon Bay: a rapidly changing coastal environment

#### 413 5.1.1. Lateral and vertical evolution of the saltmarshes

414 Results have underlined a rapid progradation and aggradation of the saltmarshes in the Aiguillon Bay,  
415 at both multi-annual and multi-decadal scales.

416 The reconstructed evolution of the saltmarsh boundary revealed a lateral expansion of the marsh up  
417 to  $14 \text{ m yr}^{-1}$ , with a mean area gain of  $8 \text{ ha yr}^{-1}$  for the period 1950-2020 (Fig. 2). The saltmarsh  
418 boundary progressively recovered a general round shape, which contrasted with a more angular  
419 morphology induced by the most recent land claims in 1963 and 1965 (Fig. 3). At a smaller spatial scale,  
420 vegetated tips up to 300 m in length are clearly evidenced along the levees on both sides of the  
421 channels. These vegetated tips can act as barriers, providing a calmer environment conducive to  
422 sediment deposition, thus favoring the gradual expansion of the saltmarsh boundary (Fagherazzi et al.,  
423 2012; Verger, 2009). It is well established that halophytic vegetation canopy can reduce waves,  
424 currents and the associated bed shear stresses (Fagherazzi et al., 2020; Lavaud et al., 2020), which in  
425 turn can have profound impact on sedimentation patterns by increasing sediment trapping efficiency  
426 (Mudd et al., 2010; Temmerman et al., 2005).

427 Sediment core data revealed vertical accretion rates of  $0.8\text{-}2.2 \text{ cm yr}^{-1}$  (Fig. 4, 5; Table 1). Multi-decadal  
428 sediment accumulation rates (SAR) were estimated using  $^{210}\text{Pb}$ -based dating models developed for  
429 each sediment core (Fig. 4; Table 1). The log profiles of  $^{210}\text{Pb}$  activity showed a linear decrease through  
430 depth below the surface mixed layer, with consistent initial activity found among all cores (Arias-Ortiz  
431 et al., 2018). The  $^{137}\text{Cs}$  profiles were coherent with the  $^{210}\text{Pb}$  models for each core, with a clear  $^{137}\text{Cs}$   
432 peak interpreted as the year 1963 found in AIG21\_22. It should be noted that an anomalous drop in  
433  $^{210}\text{Pb}$  activity was found in the AIG21\_22 profile at c. 50 cm depth, and dated to  $1970 \pm 4 \text{ yrs}$ . Both a  
434 remobilization of older material and/or a higher sediment accumulation diluting the  $^{210}\text{Pb}$  signal could  
435 explain a decrease in  $^{210}\text{Pb}$  activity (Nolte et al., 2013). A possible explanation includes the  
436 remobilization of mudflat sediment by storm waves and its transport toward saltmarshes during  
437 marine flooding. Although no marine flooding event was reported for this period in the studied area  
438 (Breilh et al., 2014), a powerful storm occurred the 13 and 14 February of 1972. Wind gusts reached  
439  $140 \text{ km h}^{-1}$  in La Rochelle, and a 89 cm-high storm surge was recorded at low tide in the mouth of the  
440 Loire Estuary, 130 km northwestward of the Aiguillon Bay ([https://www.bretagne.developpement-](https://www.bretagne.developpement-durable.gouv.fr/etude-vimers-des-evenements-de-tempete-en-bretagne-a2705.html)  
441 [durable.gouv.fr/etude-vimers-des-evenements-de-tempete-en-bretagne-a2705.html](https://www.bretagne.developpement-durable.gouv.fr/etude-vimers-des-evenements-de-tempete-en-bretagne-a2705.html),  
442 <http://tempetes.meteo.fr>). Another possibility relates to the construction of embankments associated  
443 with the most recent land claim in 1965. Indeed, embankments are built of mud that is partly dug from  
444 the saltmarsh, which can lead to significant remobilization of old sediment material potentially  
445 redeposited in the vicinity of the coring site.

446 Multi-decadal sediment accumulation rates in the saltmarshes of the Aiguillon Bay ( $0.8\text{-}2.2 \text{ cm yr}^{-1}$ ) are  
447 among the highest reported for equivalent systems found in temperate regions (Giuliani and Bellucci,  
448 2019; Fig. 6). In particular, SAR of the Aiguillon Bay exceed the global SAR value of  $2.4 \pm 0.5 \text{ mm yr}^{-1}$   
449 reported for saltmarshes (Ouyang et al., 2022). LiDAR data for the period 2010-2021 tend to confirm  
450 the SAR orders of magnitude at the coring locations ( $1.2\text{-}2.9 \text{ cm yr}^{-1}$ ; Fig. 5b). Besides relatively high  
451 uncertainty in the vertical accuracy of the LiDAR DEM data, the consistency between the two  
452 techniques strengthens the reliability of SAR estimates from the cores. High sedimentation rates may  
453 appear surprising regarding the small size and the small water discharge of the rivers flowing in or close  
454 to the bay ( $2 \text{ m}^3 \text{ s}^{-1}$  for the Lay River, and  $12 \text{ m}^3 \text{ s}^{-1}$  for the Sèvre Niortaise River; Banque HYDRO,  
455 1969/2017). Like in the Aiguillon Bay, very high sedimentation rates were also reported for the

456 Marennes-Oléron Bay, located 45 km to the south (Allard et al., 2010; Bertin et al., 2005; Bertin and  
457 Chaumillon, 2006; Poirier et al., 2016; Fig. 1). Four main sources of fine-grained sediment explain the  
458 rapid sediment-fill of the Marennes-Oléron Bay, including: (i) small coastal rivers flowing directly into  
459 the area; (ii) the Gironde estuary (to the south; Fig. 1); (iii) Mesozoic marls and limestones outcropping  
460 along the coast; and (iv) coastal marsh sediments. The Gironde estuary alone was found to account for  
461 up to 84 % of the sediment supplied to the Marennes-Oléron Bay (Dabrin et al., 2014). By analogy, it  
462 can be proposed that the sediment-fill of the Aiguillon Bay is not solely derived from the local rivers  
463 flowing close to or within the cove. The relative contribution of sediment supplied by the Gironde  
464 Estuary and by erosion of coastal marls and limestones remains unknown, but cannot be excluded.

465 Beyond the control by sediment supply, high sedimentation rates in the Aiguillon Bay can be related  
466 to both its morphology and history. The presence of a few kilometer-long sand spit in the West (“Pointe  
467 de l'Aiguillon”; Fig. 1) makes this bay a sheltered environment that prevents erosion and favors siltation  
468 (Verger, 2009). Also, the Aiguillon Bay inherited from a long history of land reclamation (Godet et al.,  
469 2015; Godet and Thomas, 2013); Fig. 1). This likely had led to a decrease in tidal prism favoring  
470 sediment deposition, itself inducing tidal prism decrease through a positive feedback mechanism  
471 (Ladd, 2021; Unger et al., 2016).

#### 472 5.1.2. Spatial heterogeneity in saltmarsh vertical evolution

473 Sedimentation rates obtained from the sediment core analysis showed an increasing trend along the  
474 two cross-shore transects, from shoreward to seaward locations (Fig 5). Also, SAR estimates did not  
475 differ significantly from the northern to the eastern transects, suggesting that the intra-site variability  
476 cannot be attributed to the proximity with the Sèvre Niortaise River. Instead, LiDAR mapping confirms  
477 the shoreward to seaward trend in SAR, with maxima found at the mudflat-saltmarsh transition, and  
478 on both sides of tidal channels and tidal creeks (Fig 5a).

479 Two main parameters can explain this spatial pattern: (i) the distance from the sediment source; and  
480 (ii) the duration of inundation, in turn related to the accommodation space between the marsh  
481 topography and the highest tide levels. Indeed, a longer and more frequent flooding of seaward areas  
482 of the saltmarsh may enhance sediment supply and deposition close to the sediment source provided  
483 by mudflats and tidal channels (Fagherazzi et al., 2020, 2012). In particular, the multi-year transects of  
484 the Aiguillon Bay illustrate the control of marsh evolution by accommodation space (Fig. 5b). The  
485 marsh topography seaward was under the mean high water springs (MHWS) in 2010. Six years later,  
486 this same zone was above MHWS showing the rapid sediment-fill of this accommodation space (Fig.  
487 5b). Then, this topography stabilized between 2016 and 2021 revealing a weak sedimentation as  
488 accommodation space reduced considerably. The same applies at the scale of the entire bay.  
489 Sedimentation rates inferred from LiDAR were maximal for the period 2010-2021 ( $1.17 \pm 0.38 \text{ cm yr}^{-1}$ )  
490 and progressively decreased towards the most recent period 2016-2021 ( $0.39 \pm 0.49 \text{ cm yr}^{-1}$ ; Table 2).  
491 It is well established that young and low-elevation saltmarshes rapidly expand up to an equilibrium  
492 elevation relative to highest water levels, while older and higher saltmarshes tend to maintain this  
493 equilibrium level (Temmerman et al., 2004; Unger et al., 2016). Zhang et al. (2019) also showed that  
494 sediment deposition on marsh platforms decreases exponentially with distance from the channels and  
495 from the marsh edge, as a function of decreasing water depth and sediment settling velocity landward.

496 It should also be noted that the most terrestrial zone of the northern saltmarsh is characterized by  
497 relatively lower elevations (i.e.,  $< 2.7 \text{ m NGF}$ ) located at a distance of 0 to 250 m from the embankment  
498 (northern transect; Fig. 5). This depression contrasts with the inner part of the eastern transect where  
499 the marsh topography gradually increases landward (Fig. 5b). Extensive and motorized mowing activity  
500 takes place in the northern bay (Godet et al., 2015; Joyeux et al., 2014), which is likely responsible for  
501 localized sediment compaction. This area also exhibits relatively high LiDAR-based SAR values (Fig. 5a).

502 They can be explained by both relatively large accommodation space, and by important sediment  
503 supply favored by the presence of gullies used to drain and clean out the mown zones.

#### 504 5.1.3. The coastal marsh evolution offsets sea level rise impact

505 The combined approach based on sediment cores and LiDAR to estimate sedimentation rates sheds  
506 light on the response of saltmarshes to sea level rise over the last decades. It provides important clues  
507 on marsh resilience, with the mean accretion rates that largely outperform the local mean sea level  
508 rise of  $2.80 \pm 0.73$  mm yr<sup>-1</sup> recorded in La Rochelle harbors (period 1993-2018, Fig. 1; Dodet et al.,  
509 2019; SONEL database, <http://www.sonel.org>). This suggests that the saltmarshes of the Aiguillon Bay  
510 are currently able to keep up with rising sea level. This has important implications with regards to  
511 services expected from such ecosystems, through adaptation to global sea level rise, protection from  
512 marine flood and shoreline erosion, and the support of ecosystem health and biodiversity (Bij de Vaate  
513 et al., 2020; Leonardi et al., 2018).

514 Interestingly, our data indicate positive accretion balance (accretion rate minus local sea-level rise  
515 rate) at both long and shorter term (Fig. 5b; Table 1, 2). This positive accretion balance in the Aiguillon  
516 Bay is consistent with what was observed in some other European sites (e.g., Silva et al., 2013), the  
517 Canadian Atlantic Coast and in the Gulf of Mexico (Crosby et al., 2016; Fig. 6). Sediment accumulation  
518 rates can vary greatly between marshes, which is explained by complex interactions between changes  
519 in relative sea level rise, tidal exchanges, vegetation type and density, and depositional processes  
520 (Giuliani and Bellucci, 2019). For instance, macrotidal marshes hold greater capacity to buffer rising  
521 sea level than microtidal ones, especially under high concentration of suspended sediment adjacent  
522 to the marsh (Friedrichs and Perry, 2022). Although it was not possible to detect storm events due to  
523 the relatively low resolution of the <sup>210</sup>Pb profiles (with the exception of the hypothetical record of the  
524 1972 storm), the history of intense and frequent storm events on the French Atlantic coast could have  
525 also favored marsh elevation (six events between 1924 and 2010; Breihl et al., 2014). During major  
526 marine flood events, tidal flats are eroded by storm waves and mud is transported and deposited  
527 shoreward onto saltmarshes and backshore environments (Baumann et al., 2017; Schuerch et al.,  
528 2018, 2013). The nature of inorganic sediment supplied to the saltmarshes during tides and storms are  
529 thus similar (e.g., grain size, TOC content). In this context, the wide mudflats of the Aiguillon Bay (3700  
530 ha) provide a substantial source of erodible fine-grained material made available for supplying the  
531 saltmarshes during high tides and storm events.

#### 532 5.2. Carbon accumulation rates in the saltmarshes

533 Organic carbon accumulation rates (CAR) calculated using the sediment cores of the Aiguillon Bay  
534 saltmarshes range from 107 to 373 g cm<sup>-2</sup> yr<sup>-1</sup>; these values are consistent with the reviewed mean  
535 CAR value of  $245 \pm 26$  g cm<sup>-2</sup> yr<sup>-1</sup> (Ouyang and Lee, 2014; Regnier et al., 2022; Fig. 6b). Given the rather  
536 low sediment OC content (1.3-6.0 %), it is very likely that these relatively high organic carbon  
537 accumulation rates are related to the fast sedimentation within saltmarshes of this bay. Similarly,  
538 Mueller et al., (2019) showed that long-term OC sequestration rates in minerogenic saltmarshes were  
539 primarily determined by sediment accumulation rates and to a far lesser degree by the variability in  
540 OC content. Results from the Aiguillon Bay will thus help refine blue carbon review efforts (Chmura et  
541 al., 2003; Duarte et al., 2005; Mcleod et al., 2011; Murray et al., 2011; Ouyang and Lee, 2014; Regnier  
542 et al., 2022), which till now, were fed by only one French study from Mediterranean estuarine  
543 saltmarshes (Hensel et al., 1999).

544 Our results also highlight an important spatial variability in OC accumulation capacity. This capacity is  
545 maximal for seaward and intermediate areas of the saltmarsh (340 g cm<sup>-2</sup> yr<sup>-1</sup> and 373 g cm<sup>-2</sup> yr<sup>-1</sup>,  
546 respectively), minimal landward (107 g cm<sup>-2</sup> yr<sup>-1</sup>), and in-between closer to the mouth of the Sèvre

547 Niortaise River ( $182 \text{ g cm}^{-2} \text{ yr}^{-1}$ ; Table 1). This variability questions the use of a unique CAR value in  
548 world review efforts, which should be best supported by multiple coring (e.g., Young et al., 2018). The  
549 heterogeneity in mass accumulation rates, used in the calculation of carbon accumulation rates, seem  
550 to be the main driver of the CAR spatial variability. This has important implications for estimating and  
551 upscaling OC accumulation rates for the studied region.

### 552 **5.3. Particulate organic carbon source and stability**

553 Van de Broek et al., (2018) stressed the fact that there might not be direct links between high OC  
554 deposition rates and high OC sequestration rates due to: (i) a potential source of allochthonous OC  
555 that is not sequestered in-situ, thus not contributing to the active removal of  $\text{CO}_2$  from the atmosphere;  
556 and (ii) OC decomposition at the surface of the marsh that can directly relates to the release of  $\text{CO}_2$   
557 and  $\text{CH}_4$  gasses. Here, we discuss these two processes to account for to avoid overestimating saltmarsh  
558 OC sequestration rates (Leorri et al., 2018).

#### 559 5.3.1. Autochthonous vs. allochthonous organic carbon

560 Sediment organic carbon in saltmarshes have two sources: (i) autochthonous OC derived from roots,  
561 woody tissues and leaf litter (supplied by C3 and C4 marsh terrestrial vegetation); and (ii)  
562 allochthonous OC produced from external sources (land and marine) and trapped by the vegetation of  
563 the marsh (Krauss et al., 2018; Van de Broek et al., 2018). The main sources of sediment to the Aiguillon  
564 Bay have distinctly different  $\delta^{13}\text{C}$  and N/C compositions, which theoretically enables interpreting the  
565 origin of OC to the saltmarshes (Fig. 7).

566  $\delta^{13}\text{C}$  and N/C within surface and near-surface sediments show a terrestrial plant signature. The  
567 signature of surface samples from the landward site (AIG21\_22) tends toward a C3 vascular-plant  
568 signature, and towards a C4 plant signature for the seaward site (AIG21\_20) (Lamb et al., 2006; Fig. 7).  
569 Plant associations mapped by the National Natural Reserve support these results, with C3 plants such  
570 as Sea Purslane (*halimione portulacoides*) dominating landward areas of the salt marshes, and C4  
571 plants like Marine Spartina (*spartina maritima*) developing preferentially seaward (Fig. S1). Previous  
572 studies similarly showed that C3 vascular vegetation can contribute largely to the organic carbon pool  
573 of supra-tidal sediments in minerogenic marshes (Wilson et al., 2005).

574 Contrasting with surface sediments, a marine source clearly dominates the OC signature of the deepest  
575 sediment samples (marine POC:  $\delta^{13}\text{C} = -25.1$  to  $-20.9 \text{ ‰}$ ; N/C = 0.13 to 0.24; SOMLIT station, Pertuis  
576 Antioche; Fig. 1a, Fig., 7). This marine signature strongly supports our interpretation that basal-core  
577 samples correspond to mudflat sediments ( $\delta^{13}\text{C} = -22.0 \pm 0.2 \text{ ‰}$ ; N/C =  $0.15 \pm 0.01$ ). Overlying these  
578 mudflat sediments, the saltmarsh sediment sections with stable OC are also placed within the range  
579 of the marine POC signature, but they differ significantly from the mudflat samples ( $\delta^{13}\text{C} = -23.5 \pm 0.4$   
580  $\text{‰}$  for AIG21\_22,  $\delta^{13}\text{C} = -21.6 \pm 0.6 \text{ ‰}$  for AIG21\_20; N/C of  $0.13 \pm 0.01$ ; Fig. 7). First, this suggests that  
581 the sediment composition of stable-OC sections is controlled primarily by the supply of allochthonous  
582 OC of marine origin. Although primary production by plants can exceed allochthonous OC deposition  
583 in some minerogenic marshes, Tidally-derived particulate organic matter is for most cases the  
584 dominant source of organic material in minerogenic marshes (e.g., Lamb et al., 2006). Second, the  
585 different signature between mudflat and saltmarsh samples also suggests that a small part of in-situ  
586 produced biomass still accounts for the stable OC content of deep saltmarsh samples.

587 In an analogous study from minerogenic marshes in northern Belgium, Van de Broek et al., (2018)  
588 discriminated: (i) a short-term OC deposition composed of relatively labile OC originating from locally-  
589 produced biomass; and (ii) a long-term OC deposition controlled by the supply of stable allochthonous  
590 OC from a marine origin. These authors further demonstrated that autochthonous OC was the main  
591 component being mineralized upon burial. The same process likely explains the transitional signature



592 of Aiguillon sediments with depth: from a terrestrial plant signature towards a signature comparable  
593 to marine POC. Interestingly, our data suggests that this mechanism applies disregarding the surface  
594 plant composition (C3 or C4).

### 595 5.3.2. Sediment organic carbon stability

596 Sediment accumulation rates from the Aiguillon saltmarshes were estimated from the stable OC  
597 sections of each core corresponding to a systematic depth below c. 20 cm and overlying mudflat  
598 sediments. Although no data are available from pore water geochemistry (e.g., Koretsky et al., 2008;  
599 Yau et al., 2022), this section of the cores was considered as the effectively-preserved OC stock  
600 (Mueller et al., 2019; Fig. 3). Steep decline in OC content with sediment depth was associated with a  
601 significant  $\delta^{13}\text{C}$  change of c. 4 ‰; enriched with depth for C3-dominated sites, and depleted for C4-  
602 dominated sites (Fig. 8a). This change was interpreted as OC loss between topsoil layers and deeper  
603 levels of the cores through sustained decomposition, with  $\delta^{13}\text{C}$  enrichment or depletion that depends  
604 on plant species and tissue types (Kelleway et al., 2022).

605 To support this interpretation and assess the  $\delta^{13}\text{C}$  signature of the reactive carbon in Aiguillon  
606 sediments, we followed the approach developed by Komada et al., (2022). It is based on the  
607 assumption that total OC in a sample ( $C_s$ ) consists of two components: a reactive ( $C_r$ ) and a non-reactive  
608 ( $C_{nr}$ ), with each component having a fixed  $\delta^{13}\text{C}$  value  $\delta_r$  and  $\delta_{nr}$ , respectively. With  $\delta_s$  the  $\delta^{13}\text{C}$  value of  
609 total OC in the sample, the following formula can be defined:

$$610 \quad C_s = C_r + C_{nr} \quad (1)$$

$$611 \quad \delta_s C_s = \delta_r C_r + \delta_{nr} C_{nr} \quad (2)$$

612 Combining (1) and (2) to replace  $C_r$ , this gives the following:

$$613 \quad \delta_s C_s = \delta_r C_s + C_{nr}(\delta_{nr} - \delta_r) \quad (3)$$

614 if  $\delta_{nr}$  and  $\delta_r$  are constant, then plotting  $\delta_s C_s$  against  $C_s$  of the samples should yield a straight line with  
615 slope equivalent to  $\delta_r$ . This approach applied to Aiguillon sediments indicates a  $\delta^{13}\text{C}$  signature of -  
616 28.1‰ and -12.2‰ for the reactive carbon ( $\delta_r$ ) related to surface C3 and C4 plants, respectively (Fig.  
617 8b). Together with the averaged  $\delta^{13}\text{C}$  signature of mudflat samples of  $-22.0 \pm 0.2$  ‰, these results  
618 suggest that surface sediments from the Aiguillon Bay are composed predominantly of reactive OC  
619 (Fig. 8). Thus, it justifies discarding the upper c. 20 cm in the calculation of OC accumulation rates, at  
620 risk of largely overestimating the carbon sink capacity of Aiguillon saltmarshes.

621 Possible explanations for changes in OC and  $\delta^{13}\text{C}$  with depth include the preferential decomposition of  
622 autochthonous vs. allochthonous OC through highly oxidizing conditions near the surface (Mueller et  
623 al., 2019), preferential use of a labile OC pool by microbial decomposers and fungi (Menichetti et al.,  
624 2015), and  $\delta^{13}\text{C}$  fractionation between above- and below-ground biomass (Benner et al., 1987). This  
625 last process is unlikely regarding the consistent  $\delta^{13}\text{C}$  signature between C3 terrestrial plants  
626 (-21 to -32 ‰), C3 below-ground biomass in Aiguillon sediments ( $-27.0 \pm 0.8$  ‰), and the signature of  
627 reactive OC calculated for marsh sediments influenced by C3 vegetation (-27.9 ‰; Fig 7, 8a).

### 628 5.4. Implications for carbon sequestration

629 Overall, our results of  $\delta^{13}\text{C}$  and N/C from the Aiguillon Bay support previous findings that allochthonous  
630 carbon of marine origin prevails in long-term OC accumulation of minerogenic marshes (e.g., Mueller  
631 et al., 2019; Van de Broek et al., 2018). Although the surface OC pool is for the most part of  
632 autochthonous origin, only a small fraction remains preserved with sediment depth, thus contributing  
633 to long-term carbon sequestration in the Aiguillon saltmarshes, which rate average  $2.5 \text{ Mg C ha}^{-1} \text{ yr}^{-1}$ .

634 Although the implications for C-crediting approaches has yet to be clarified (e.g., Mueller et al., 2019),  
635 the ability of coastal ecosystems to trap and store large amounts of allochthonous carbon from  
636 adjacent ecosystems remains a major asset with respect to the carbon sink function (e.g., Jennerjahn,  
637 2020). Our results imply that the wealth of the long-term carbon sequestration rates in minerogenic  
638 coastal marshes does not only depend on the marsh morphological evolution and the OC burial  
639 capacity of the vegetation. It also depends on the quality of coastal ecosystems at a larger scale, which  
640 includes nearshore waters and mudflat primary productivity. This calls on the need for more  
641 integrative coastal science, in which saltmarshes are considered as part of a coupled mudflat-marsh  
642 system, for instance (Schuerch et al., 2019). This coupling was emphasized among the top-ten pending  
643 questions to help prioritize the future of blue carbon science (Macreadie et al., 2019).

644 **6. Conclusions**

645 The saltmarshes of the Aiguillon Bay have shown great ability to cope with sea level rise, by elevating  
646 their topography at rates among the highest reported worldwide for these depositional environments.  
647 Our results highlighted the key role of sedimentation in providing and in maintaining ecosystem  
648 services offered by coastal wetlands. At present, the Aiguillon Bay still holds relatively important  
649 accommodation space, which enables it to expand both laterally and vertically at significant rates. The  
650 study site has inherited a long history of considerable sediment-fill of the Marais Poitevin, and it is still  
651 today characterized by significant sediment accumulation rates and volume gains. This suggests  
652 encouraging conditions for the resilience of the saltmarshes of the Aiguillon Bay in the face of future  
653 climate change and sea level rise. Nevertheless, as the source of sediment is not known precisely and  
654 in what quantity, it remains difficult to predict the future evolution of saltmarshes in the bay.

655 Our findings support previous research showing that marine-derived carbon dominates long-term  
656 organic carbon accumulation in minerogenic coastal marshes, while only a small fraction of locally-  
657 produced carbon is preserved deeper in the sediment. This suggests that carbon accumulation rates in  
658 these saltmarshes depend not only on marsh morphology and vegetation's carbon burial capacity but  
659 also on the broader coastal ecosystem, including nearshore waters and mudflat productivity.  
660 Integrative coastal science, viewing saltmarshes as part of a coupled mudflat-marsh system, appears  
661 essential to better understand carbon dynamics and sequestration rates in these coastal wetlands.

662 Increasing the value and recognition of the key role of intertidal ecosystems were also suggested as a  
663 potential lever to help sustain high biological production in coastal ecosystems. In particular, raising  
664 public awareness through communication of scientific knowledge can play an important role for  
665 integrating adaptation and mitigation options (IPCC, 2022). Among the multiple supports,  
666 popularization of science intended for the general public have shown to be particularly efficient in this  
667 regard (Chaumillon et al., 2019, 2021; <https://pnr.parc-marais-poitevin.fr/la-mer-contre-attaque-le-nouveau-show-scientifique-debarque-a-la-rochelle-mardi-26-novembre-2019>). Another way to  
668 increase the value of intertidal ecosystems is through the prism of natural heritage. The  
669 transdisciplinary consortia in which this study is framed by (ANR Project PAMPAS: *'Evolution of the*  
670 *Heritage Identity of the Pertuis Charentais marshes in response to the hazard of marine submersion'*),  
671 may enable to open such perspectives.  
672

673 **Acknowledgment**

674 This work was financed by two transdisciplinary consortia that are the ANR project PAMPAS (# ANR-  
675 18-CE32-0006-01) and La Rochelle Territoire Zero Carbone (LRTZC, Carbon Bleu Axe2 # OPE-2021-0376,  
676 # OPE-2021-0496), and supported by the LIFE project “Baie de l’Aiguillon”, LIFE14 NAT/FR/000669  
677 (January 1<sup>th</sup> 2016 -June 30 2022). We would like to thank the team of the ‘Réserve Naturelle Nationale  
678 de la Baie de l’Aiguillon’. Special thanks go to Paméla Lagrange (LPO), Régis Gallais (OFB), Jean-Pierre  
679 Guéret (LPO), and Frédéric Robin (LPO) for their support with fieldwork, for sharing their expertise,  
680 and for data access. We are also grateful to Laurent Godet (LETG, Nantes University) for sharing  
681 georeferenced data about the historical land claims and evolution of the saltmarsh boundary in the  
682 Aiguillon Bay. Particular thanks go to Christophe Petit (ArScAn, University Paris 1) and Vincent Bichet  
683 (ChronoEnvironnement, UBFC) for their support with fieldwork material, and to Aurélie Pace, and  
684 Jasson Mora Mussio (LIENSs, CNRS-La Rochelle University) for their help with the coring field  
685 campaigns. We would like also to thank Guillou Gaël and Benoit Lebreton (LIENSs, CNRS-La Rochelle  
686 University) for their support with the IRMS platform. Special thanks go to Christine Dupuy for her  
687 support and Anaïs Schmitt (LIENSs, CNRS-La Rochelle University) for active discussion about the  
688 sediment dynamics of the Gironde estuary and Pertuis sea Marine Nature Park (CELHYSE Project).

689 **References**

- 690 Allard, J., Chaumillon, E., Bertin, X., Poirier, C., Ganthy, F., 2010. Sedimentary record of  
691 environmental changes and human interferences in a macrotidal bay for the last millenaries:  
692 the Marennes-Oléron Bay (SW France). *Bull. Société Géologique Fr.* 181, 151–169.  
693 <https://doi.org/10.2113/gssgfbull.181.2.151>
- 694 Arias-Ortiz, A., Masqué, P., Garcia-Orellana, J., Serrano, O., Mazarrasa, I., Marbà, N., Lovelock, C.E.,  
695 Lavery, P.S., Duarte, C.M., 2018. Reviews and syntheses:  $\text{Pb}$ -  
696 derived sediment and carbon accumulation rates in vegetated coastal ecosystems – setting  
697 the record straight. *Biogeosciences* 15, 6791–6818. [https://doi.org/10.5194/bg-15-6791-](https://doi.org/10.5194/bg-15-6791-2018)  
698 2018
- 699 Baumann, J., Chaumillon, E., Schneider, J.-L., Jorissen, F., Sauriau, P.-G., Richard, P., Bonnin, J.,  
700 Schmidt, S., 2017. Contrasting sediment records of marine submersion events related to  
701 wave exposure, Southwest France. *Sediment. Geol.* 353, 158–170.  
702 <https://doi.org/10.1016/j.sedgeo.2017.03.009>
- 703 Baustian, M.M., Stagg, C.L., Perry, C.L., Moss, L.C., Carruthers, T.J.B., Allison, M., 2017. Relationships  
704 Between Salinity and Short-Term Soil Carbon Accumulation Rates from Marsh Types Across a  
705 Landscape in the Mississippi River Delta. *Wetlands* 37, 313–324.  
706 <https://doi.org/10.1007/s13157-016-0871-3>
- 707 Benner, R., Fogel, M.L., Sprague, E.K., Hodson, R.E., 1987. Depletion of  $^{13}\text{C}$  in lignin and its  
708 implications for stable carbon isotope studies. *Nature* 329, 708–710.  
709 <https://doi.org/10.1038/329708a0>
- 710 Bertin, X., Bruneau, N., Breilh, J.-F., Fortunato, A.B., Karpytchev, M., 2012. Importance of wave age  
711 and resonance in storm surges: The case Xynthia, Bay of Biscay. *Ocean Model.* 42, 16–30.  
712 <https://doi.org/10.1016/j.ocemod.2011.11.001>
- 713 Bertin, X., Chaumillon, E., 2006. The implication of oyster farming in increasing sedimentation rates in  
714 a macrotidal bay: the Marennes-Oléron Bay, France 5.
- 715 Bertin, X., Chaumillon, E., Sottolichio, A., Pedreros, R., 2005. Tidal inlet response to sediment infilling  
716 of the associated bay and possible implications of human activities: the Marennes-Oléron  
717 Bay and the Maumusson Inlet, France. *Cont. Shelf Res.* 25, 1115–1131.  
718 <https://doi.org/10.1016/j.csr.2004.12.004>
- 719 Bertin, X., Li, K., Roland, A., Zhang, Y.J., Breilh, J.F., Chaumillon, E., 2014. A modeling-based analysis of  
720 the flooding associated with Xynthia, central Bay of Biscay. *Coast. Eng.* 94, 80–89.  
721 <https://doi.org/10.1016/j.coastaleng.2014.08.013>
- 722 Bertram, C., Quaas, M., Reusch, T.B.H., Vafeidis, A.T., Wolff, C., Rickels, W., 2021. The blue carbon  
723 wealth of nations. *Nat. Clim. Change* 11, 704–709. [https://doi.org/10.1038/s41558-021-](https://doi.org/10.1038/s41558-021-01089-4)  
724 01089-4
- 725 Bij de Vaate, I., Brückner, M.Z.M., Kleinhans, M.G., Schwarz, C., 2020. On the Impact of Salt Marsh  
726 Pioneer Species-Assemblages on the Emergence of Intertidal Channel Networks. *Water*  
727 *Resour. Res.* 56. <https://doi.org/10.1029/2019WR025942>
- 728 Breilh, J.-F., Bertin, X., Chaumillon, E., Giloy, N., Sauzeau, T., 2014. How frequent is storm-induced  
729 flooding in the central part of the Bay of Biscay? *Glob. Planet. Change* 122, 161–175.  
730 <https://doi.org/10.1016/j.gloplacha.2014.08.013>
- 731 Breilh, J.F., Chaumillon, E., Bertin, X., Gravelle, M., 2013. Assessment of static flood modeling  
732 techniques: application to contrasting marshes flooded during Xynthia (western France). *Nat.*  
733 *Hazards Earth Syst. Sci.* 13, 1595–1612. <https://doi.org/10.5194/nhess-13-1595-2013>
- 734 Chaumillon, E., Proust, J.-N., Menier, D., Weber, N., 2008. Incised-valley morphologies and  
735 sedimentary-fills within the inner shelf of the Bay of Biscay (France): A synthesis. *J. Mar. Syst.*  
736 72, 383–396. <https://doi.org/10.1016/j.jmarsys.2007.05.014>
- 737 Chaumillon, E., Tessier, B., Weber, N., Tesson, M., Bertin, X., 2004. Buried sandbodies within present-  
738 day estuaries (Atlantic coast of France) revealed by very high resolution seismic surveys. *Mar.*  
739 *Geol.* 211, 189–214.

740 Chmura, G.L., Anisfeld, S.C., Cahoon, D.R., Lynch, J.C., 2003. Global carbon sequestration in tidal,  
741 saline wetland soils. *Glob. Biogeochem. Cycles* 17, n/a-n/a.  
742 <https://doi.org/10.1029/2002GB001917>

743 Coignot, E., Polsenaere, P., Soletchnik, P., et al., 2020. Variabilité spatio-temporelle des nutriments et  
744 du carbone et flux associés le long d'un continuum terrestres-aquatique tempéré (Marais  
745 Poitevin – Baie de l'Aiguillon – Pertuis Breton). Rapport final (suivi 2017-2018), IFREMER.  
746 Archived in : ARCHIMER Ifremer's institutional repository.

747 Collin, A., Long, B., Archambault, P., 2010. Salt-marsh characterization, zonation assessment and  
748 mapping through a dual-wavelength LiDAR. *Remote Sens. Environ.* 114, 520–530.  
749 <https://doi.org/10.1016/j.rse.2009.10.011>

750 Constantin, S., Doxaran, D., Derkacheva, A., Novoa, S., Lavigne, H., 2018. Multi-temporal dynamics of  
751 suspended particulate matter in a macrotidal river Plume (the Gironde) as observed by  
752 satellite data. *Estuar. Coast. Shelf Sci.* 202, 172-184.  
753 <https://doi.org/10.1016/j.ecss.2018.01.004>

754 Corbett, D.R., Walsh, J.P., 2015. <sup>210</sup>Lead and <sup>137</sup>Cesium: establishing a chronology for the last  
755 century, in: Shennan, I., Long, A.J., Horton, B.P. (Eds.), *Handbook of Sea-Level Research*. John  
756 Wiley & Sons, Ltd, Chichester, UK, pp. 361–372.  
757 <https://doi.org/10.1002/9781118452547.ch24>

758 Costanza, R., de Groot, R., Sutton, P., van der Ploeg, S., Anderson, S.J., Kubiszewski, I., Farber, S.,  
759 Turner, R.K., 2014. Changes in the global value of ecosystem services. *Glob. Environ. Change*  
760 26, 152–158. <https://doi.org/10.1016/j.gloenvcha.2014.04.002>

761 Craft, C.B., Seneca, E.D., Broome, S.W., 1991. Loss on Ignition and Kjeldahl Digestion for Estimating  
762 Organic Carbon and Total Nitrogen in Estuarine Marsh Soils: Calibration with Dry  
763 Combustion. *Estuaries* 14, 175. <https://doi.org/10.2307/1351691>

764 Crosby, S.C., Sax, D.F., Palmer, M.E., Booth, H.S., Deegan, L.A., Bertness, M.D., Leslie, H.M., 2016. Salt  
765 marsh persistence is threatened by predicted sea-level rise. *Estuar. Coast. Shelf Sci.* 181, 93–  
766 99. <https://doi.org/10.1016/j.ecss.2016.08.018>

767 Dabrin, A., Schäfer, J., Bertrand, O., Masson, M., Blanc, G., 2014. Origin of suspended matter and  
768 sediment inferred from the residual metal fraction: Application to the Marennes Oleron Bay,  
769 France. *Cont. Shelf Res.* 72, 119–130. <https://doi.org/10.1016/j.csr.2013.07.008>

770 DataLab France, 2022. Chiffres clés du climat: France, Europe et Monde. Ministère de la Transition  
771 écologique, France. [https://www.statistiques.developpement-durable.gouv.fr/edition-](https://www.statistiques.developpement-durable.gouv.fr/edition-numerique/chiffres-cles-du-climat-2022/avant-propos)  
772 [numerique/chiffres-cles-du-climat-2022/avant-propos](https://www.statistiques.developpement-durable.gouv.fr/edition-numerique/chiffres-cles-du-climat-2022/avant-propos).

773 Dodet, G., Bertin, X., Bouchette, F., Gravelle, M., Testut, L., Wöppelmann, G., 2019. Characterization  
774 of Sea-level Variations Along the Metropolitan Coasts of France: Waves, Tides, Storm Surges  
775 and Long-term Changes. *J. Coast. Res.* 88, 10. <https://doi.org/10.2112/S188-003.1>

776 Doxaran, D., Froidefond, J-M., Castaing, P., Babin, M., 2009. Dynamics of the turbidity maximum zone  
777 in a macrotidal estuary (the Gironde, France): Observations from field and MODIS satellite  
778 data. *Estuar. Coast. Shelf Sci.* 81, 321–332. <https://doi:10.1016/j.ecss.2008.11.013>.

779 Duarte, C.M., Middelburg, J.J., Caraco, N., 2005. Major role of marine vegetation on the oceanic  
780 carbon cycle 8.

781 Dubosq, N., Schmidt, S., Walsh, J.P., Grémare, A., Gillet, H., Lebleu, P., Poirier, D., Perello, M.-C.,  
782 Lamarque, B., Deflandre, B., 2021. A first assessment of organic carbon burial in the West  
783 Gironde Mud Patch (Bay of Biscay). *Cont. Shelf Res.* 221, 104419.  
784 <https://doi.org/10.1016/j.csr.2021.104419>

785 Dupuy C., Agogué H., Amann B., Azémar F., Becu N., et al., 2022. Towards carbon neutrality by 2040  
786 in La Rochelle metropolitan area (France): quantifying the role of wetlands and littoral zone  
787 in the capture and sequestration of blue carbon. ECSA 59: Using the best scientific  
788 knowledge for the sustainable management of estuaries and coastal seas will take place in  
789 San Sebastian, Spain from 5-8 September 2022. hal-03777579

790 Fagherazzi, S., Kirwan, M.L., Mudd, S.M., Guntenspergen, G.R., Temmerman, S., D'Alpaos, A., van de  
791 Koppel, J., Rybczyk, J.M., Reyes, E., Craft, C., Clough, J., 2012. Numerical models of salt marsh

792 evolution: Ecological, geomorphic, and climatic factors. *Rev. Geophys.* 50, RG1002.  
793 <https://doi.org/10.1029/2011RG000359>

794 Fagherazzi, S., Mariotti, G., Leonardi, N., Canestrelli, A., Nardin, W., Kearney, W.S., 2020. Salt Marsh  
795 Dynamics in a Period of Accelerated Sea Level Rise. *J. Geophys. Res. Earth Surf.* 125.  
796 <https://doi.org/10.1029/2019JF005200>

797 Ford, M., 2012. Shoreline Changes on an Urban Atoll in the Central Pacific Ocean: Majuro Atoll,  
798 Marshall Islands. *J. Coast. Res.* 279, 11–22. <https://doi.org/10.2112/JCOASTRES-D-11-00008.1>

799 Friedrichs, C.T., Perry, J.E., 2022. Tidal Salt Marsh Morphodynamics: A Synthesis 32.

800 Giuliani, S., Bellucci, L.G., 2019. Salt Marshes: Their Role in Our Society and Threats Posed to Their  
801 Existence, in: *World Seas: An Environmental Evaluation*. Elsevier, pp. 79–101.  
802 <https://doi.org/10.1016/B978-0-12-805052-1.00004-8>

803 Godet, L., Pourinet, L., Joyeux, E., Verger, F., 2015. Dynamique spatiale et usage des schorres de  
804 l’Anse de l’Aiguillon de 1705 à nos jours. *Enjeux de conservation d’un patrimoine naturel*  
805 littoral marin. *Cybergeo*. <https://doi.org/10.4000/cybergeo.26774>

806 Godet, L., Thomas, A., 2013. Three centuries of land cover changes in the largest French Atlantic  
807 wetland provide new insights for wetland conservation. *Appl. Geogr.* 42, 133–139.  
808 <https://doi.org/10.1016/j.apgeog.2013.05.011>

809 Hendriks, K., Gubbay, S., Arets, E., Janssen, J., 2020. Carbon storage in European ecosystems: a quick  
810 scan for terrestrial and marine EUNIS habitat types. Wageningen, Wageningen  
811 Environmental Research, Internal Report. 66 pp. 87.

812 Hensel, P.F., Day Jr., J.W., Pont, D., 1999. Wetland Vertical Accretion and Soil Elevation Change in the  
813 Rhone River Delta, France: The Importance of Riverine Flooding. *J. Coastal Res.* 15, 668–681.

814 Himes-Cornell, A., Pendleton, L., Atiyah, P., 2018. Valuing ecosystem services from blue forests: A  
815 systematic review of the valuation of salt marshes, sea grass beds and mangrove forests.  
816 *Ecosyst. Serv.* 30, 36–48. <https://doi.org/10.1016/j.ecoser.2018.01.006>

817 Himmelstoss, E.A., Henderson, R.E., Kratzmann, M.G., Farris, A.S., 2018. Digital Shoreline Analysis  
818 System DSAS Version 5.0 User Guide.” Open-File Report 2018-1179: 126. Open-File Report  
819 1179, 126.

820 Howard, J., Hoyt, S., Insensee, K., Telszewski, M., Pidgeon, E., 2014. Coastal Blue Carbon: Methods for  
821 assessing carbon stocks and emissions factors in mangroves, tidal salt marshes, and  
822 seagrasses. Conservation International, Intergovernmental Oceanographic Commission of  
823 UNESCO, International Union for Conservation of Nature, Arlington, Virginia, USA.

824 IPCC, 2022. Climate Change 2022: Mitigation of Climate Change. Skea et al., Working Group III  
825 contribution to the Sixth Assessment Report of the Intergovernmental Panel on Climate  
826 Change. Summary for Policymakers 99.

827 Iurian, A.R., Millward, G., Blake, W., Abril Hernández, J.M., 2021. Fine-tuning of 210Pb-based  
828 methods for dating vegetated saltmarsh sediments. *Quat. Geochronol.* 62, 101153.  
829 <https://doi.org/10.1016/j.quageo.2021.101153>

830 Jennerjahn, T.C., 2020. Relevance and magnitude of “Blue Carbon” storage in mangrove sediments:  
831 Carbon accumulation rates vs. stocks, sources vs. sinks. *Estuar. Coast. Shelf Sci.* 247, 107027.  
832 <https://doi.org/10.1016/j.ecss.2020.107027>

833 Joyeux, E., Blanchet, R., Haie, S., Carpentier, A., 2014. La gestion des prés salés de la baie de  
834 l’Aiguillon: vers une approche fonctionnelle. In: *Faune sauvage*, 302. 38–43.

835 Kelleway, J.J., Trevathan-Tackett, S.M., Baldock, J., Critchley, L.P., 2022. Plant litter composition and  
836 stable isotope signatures vary during decomposition in blue carbon ecosystems.  
837 *Biogeochemistry* 158, 147–165. <https://doi.org/10.1007/s10533-022-00890-3>

838 Komada, T., Bravo, A., Brinkmann, M., Lu, K., Wong, L., Shields, G., 2022. “Slow” and “fast” in blue  
839 carbon: Differential turnover of allochthonous and autochthonous organic matter in  
840 minerogenic salt marsh sediments. *Limnol. Oceanogr.* Ino.12090.  
841 <https://doi.org/10.1002/Ino.12090>

842 Koretsky, C.M., Haveman, M., Cuellar, A., Beuving, L., Shattuck, T., Wagner, M., 2008. Influence of  
843 Spartina and Juncus on Saltmarsh Sediments. I. Pore Water Geochemistry. *Chem. Geol.* 255,  
844 87–99. <https://doi.org/10.1016/j.chemgeo.2008.06.013>

845 Krauss, K.W., Noe, G.B., Duberstein, J.A., Conner, W.H., Stagg, C.L., Cormier, N., Jones, M.C.,  
846 Bernhardt, C.E., Graeme Lockaby, B., From, A.S., Doyle, T.W., Day, R.H., Ensign, S.H.,  
847 Pierfelice, K.N., Hupp, C.R., Chow, A.T., Whitbeck, J.L., 2018. The Role of the Upper Tidal  
848 Estuary in Wetland Blue Carbon Storage and Flux. *Glob. Biogeochem. Cycles* 32, 817–839.  
849 <https://doi.org/10.1029/2018GB005897>

850 Ladd, C.J.T., 2021. Review on processes and management of saltmarshes across Great Britain. *Proc.*  
851 *Geol. Assoc.* 15.

852 Lamb, A.L., Wilson, G.P., Leng, M.J., 2006. A review of coastal palaeoclimate and relative sea-level  
853 reconstructions using  $\delta^{13}\text{C}$  and C/N ratios in organic material. *Earth-Sci. Rev.* 75, 29–57.  
854 <https://doi.org/10.1016/j.earscirev.2005.10.003>

855 Lavaud, L., Lechevalier, A., Coulombier, T., Bertin, X., Martins, K., 2020. Effet de la végétation sur la  
856 dissipation des vagues au niveau d'un pré salé. XVIèmes Journées Nationales Génie Côtier –  
857 Génie Civil. Le Havre, 2020. <https://doi.org/10.5150/jngcgc.2020.010>

858 Leonardi, N., Carnacina, I., Donatelli, C., Ganju, N.K., Plater, A.J., Schuerch, M., Temmerman, S., 2018.  
859 Dynamic interactions between coastal storms and salt marshes: A review. *Geomorphology*  
860 301, 92–107. <https://doi.org/10.1016/j.geomorph.2017.11.001>

861 Leorri, E., Zimmerman, A.R., Mitra, S., Christian, R.R., Fatela, F., Mallinson, D.J., 2018. Refractory  
862 organic matter in coastal salt marshes-effect on C sequestration calculations. *Sci. Total*  
863 *Environ.* 633, 391–398. <https://doi.org/10.1016/j.scitotenv.2018.03.120>

864 Lovelock, C.E., Reef, R., 2020. Variable Impacts of Climate Change on Blue Carbon. *One Earth* 3, 195–  
865 211. <https://doi.org/10.1016/j.oneear.2020.07.010>

866 Macreadie, P.I., Anton, A., Raven, J.A., Beaumont, N., Connolly, R.M., Friess, D.A., Kelleway, J.J.,  
867 Kennedy, H., Kuwae, T., Lavery, P.S., Lovelock, C.E., Smale, D.A., Apostolaki, E.T., Atwood,  
868 T.B., Baldock, J., Bianchi, T.S., Chmura, G.L., Eyre, B.D., Fourqurean, J.W., Hall-Spencer, J.M.,  
869 Huxham, M., Hendriks, I.E., Krause-Jensen, D., Laffoley, D., Luisetti, T., Marbà, N., Masque, P.,  
870 McGlathery, K.J., Megonigal, J.P., Murdiyarso, D., Russell, B.D., Santos, R., Serrano, O.,  
871 Silliman, B.R., Watanabe, K., Duarte, C.M., 2019. The future of Blue Carbon science. *Nat.*  
872 *Commun.* 10, 3998. <https://doi.org/10.1038/s41467-019-11693-w>

873 Mcleod, E., Chmura, G.L., Bouillon, S., Salm, R., Björk, M., Duarte, C.M., Lovelock, C.E., Schlesinger,  
874 W.H., Silliman, B.R., 2011. A blueprint for blue carbon: toward an improved understanding of  
875 the role of vegetated coastal habitats in sequestering CO<sub>2</sub>. *Front. Ecol. Environ.* 9, 552–560.  
876 <https://doi.org/10.1890/110004>

877 Medeiros, S.C., Bobinsky, J.S., Abdelwahab, K., 2022. Locality of topographic ground truth data for  
878 salt marsh lidar DEM elevation bias mitigation. *IEEE J. Sel. Top. Appl. Earth Obs. Remote Sens.*  
879 1–10. <https://doi.org/10.1109/JSTARS.2022.3189226>

880 Menichetti, L., Houot, S., van Oort, F., Kätterer, T., Christensen, B.T., Chenu, C., Barré, P., Vasilyeva,  
881 N.A., Ekblad, A., 2015. Increase in soil stable carbon isotope ratio relates to loss of organic  
882 carbon: results from five long-term bare fallow experiments. *Oecologia* 177, 811–821.  
883 <https://doi.org/10.1007/s00442-014-3114-4>

884 Mudd, S.M., D'Alpaos, A., Morris, J.T., 2010. How does vegetation affect sedimentation on tidal  
885 marshes? Investigating particle capture and hydrodynamic controls on biologically mediated  
886 sedimentation. *J. Geophys. Res.* 115, F03029. <https://doi.org/10.1029/2009JF001566>

887 Mueller, P., Ladiges, N., Jack, A., Schmiedl, G., Kutzbach, L., Jensen, K., Nolte, S., 2019. Assessing the  
888 long-term carbon-sequestration potential of the semi-natural salt marshes in the European  
889 Wadden Sea. *Ecosphere* 10. <https://doi.org/10.1002/ecs2.2556>

890 Murray, B.C., Pendleton, L., Jenkins, W.A., Sifleet, S., 2011. Green Payments for Blue Carbon.  
891 Economic Incentives for Protecting Threatened Coastal Habitats Nicholas Institute for  
892 Environmental Policy Solutions Report NI R 11-04, 52.



893 Nolte, S., Koppenaar, E.C., Esselink, P., Dijkema, K.S., Schuerch, M., De Groot, A.V., Bakker, J.P.,  
894 Temmerman, S., 2013. Measuring sedimentation in tidal marshes: a review on methods and  
895 their applicability in biogeomorphological studies. *J. Coast. Conserv.* 17, 301–325.  
896 <https://doi.org/10.1007/s11852-013-0238-3>

897 Ouyang, X., Connolly, R.M., Lee, S.Y., 2022. Revised global estimates of resilience to sea level rise for  
898 tidal marshes. *Environ. Chall.* 9, 100593. <https://doi.org/10.1016/j.envc.2022.100593>

899 Ouyang, X., Lee, S.Y., 2020. Improved estimates on global carbon stock and carbon pools in tidal  
900 wetlands. *Nat. Commun.* 11, 317. <https://doi.org/10.1038/s41467-019-14120-2>

901 Ouyang, X., Lee, S.Y., 2014. Updated estimates of carbon accumulation rates in coastal marsh  
902 sediments. *Biogeosciences* 11, 5057–5071. <https://doi.org/10.5194/bg-11-5057-2014>

903 Poirier, C., Poitevin, C., Chaumillon, É., 2016. Comparison of estuarine sediment record with  
904 modelled rates of sediment supply from a western European catchment since 1500. *Comptes*  
905 *Rendus Geosci.* 348, 479–488. <https://doi.org/10.1016/j.crte.2015.02.009>

906 Regnier, P., Resplandy, L., Najjar, R.G., Ciais, P., 2022. The land-to-ocean loops of the global carbon  
907 cycle. *Nature* 603, 401–410. <https://doi.org/10.1038/s41586-021-04339-9>

908 Reyss, J.-L., Schmidt, S., Legeleux, F., Bonté, P., 1995. Large, low background well-type detectors for  
909 measurements of environmental radioactivity. *Nucl. Instrum. Methods Phys. Res.* 357, 391–  
910 397. [https://doi.org/10.1016/0168-9002\(95\)00021-6](https://doi.org/10.1016/0168-9002(95)00021-6)

911 Rogers, K., Kelleway, J.J., Saintilan, N., Megonigal, J.P., Adams, J.B., Holmquist, J.R., Lu, M., Schile-  
912 Beers, L., Zawadzki, A., Mazumder, D., Woodroffe, C.D., 2019. Wetland carbon storage  
913 controlled by millennial-scale variation in relative sea-level rise. *Nature* 567, 91–95.  
914 <https://doi.org/10.1038/s41586-019-0951-7>

915 Schuerch, M., Spencer, T., Evans, B., 2019. Coupling between tidal mudflats and salt marshes affects  
916 marsh morphology. *Mar. Geol.* 412, 95–106. <https://doi.org/10.1016/j.margeo.2019.03.008>

917 Schuerch, M., Spencer, T., Temmerman, S., Kirwan, M.L., Wolff, C., Lincke, D., McOwen, C.J.,  
918 Pickering, M.D., Reef, R., Vafeidis, A.T., Hinkel, J., Nicholls, R.J., Brown, S., 2018. Future  
919 response of global coastal wetlands to sea-level rise. *Nature* 561, 231–234.  
920 <https://doi.org/10.1038/s41586-018-0476-5>

921 Schuerch, M., Vafeidis, A., Slawig, T., Temmerman, S., 2013. Modeling the influence of changing  
922 storm patterns on the ability of a salt marsh to keep pace with sea level rise: SALT MARSH  
923 ACCRETION AND STORM ACTIVITY. *J. Geophys. Res. Earth Surf.* 118, 84–96.  
924 <https://doi.org/10.1029/2012JF002471>

925 Schmitt A., Chaumillon E., 2023. Understanding morphological evolution and sediment dynamics at  
926 multi-time scales helps balance human activities and protect coastal ecosystems: an example  
927 with the Gironde and Pertuis Marine Park. *Sci. Tot. Env.* 887, 163819

928 Silva, T.A., Freitas, M.C., Andrade, C., Taborda, R., Freire, P., Schmidt, S., Antunes, C., 2013.  
929 Geomorphological response of the salt-marshes in the Tagus estuary to sea level rise. *J.*  
930 *Coast. Res.* 65, 582–587. <https://doi.org/10.2112/SI65-099.1>

931 Stupar, Y.V., Schäfer, J., García, M.G., Schmidt, S., Piovano, E., Blanc, G., Huneau, F., Le Coustumer, P.,  
932 2014. Historical mercury trends recorded in sediments from the Laguna del Plata, Córdoba,  
933 Argentina. *Geochemistry* 74, 353–363. <https://doi.org/10.1016/j.chemer.2013.11.002>

934 Temmerman, S., Bouma, T.J., Govers, G., wang, Z.B., De Vries, M. B., Herman, P.M.J., 2005. Impact of  
935 vegetation on flow routing and sedimentation patterns: Three-dimensional modeling for a  
936 tidal marsh. *J Geophys Res* 110. <https://doi.org/10.1029/2005JF000301>

937 Temmerman, S., Govers, G., Wartel, S., Meire, P., 2004. Modelling estuarine variations in tidal marsh  
938 sedimentation: response to changing sea level and suspended sediment concentrations. *Mar.*  
939 *Geol.* 212, 1–19. <https://doi.org/10.1016/j.margeo.2004.10.021>

940 Unger, V., Eelsey-Quirk, T., Sommerfield, C., Velinsky, D., 2016. Stability of organic carbon  
941 accumulating in *Spartina alterniflora*-dominated salt marshes of the Mid-Atlantic U.S. *Estuar.*  
942 *Coast. Shelf Sci.* 182, 179–189. <https://doi.org/10.1016/j.ecss.2016.10.001>

943 Van de Broek, M., Vandendriessche, C., Poppelmonde, D., Merckx, R., Temmerman, S., Govers, G.,  
944 2018. Long-term organic carbon sequestration in tidal marsh sediments is dominated by old-

945 aged allochthonous inputs in a macrotidal estuary. *Glob. Change Biol.* 24, 2498–2512.  
946 <https://doi.org/10.1111/gcb.14089>

947 Verger, F., 2009. *Zones humides du littoral français*, Belin. ed. Paris.

948 Vinent, O.D., Johnston, R.J., Kirwan, M.L., Leroux, A.D., Martin, V.L., 2019. Coastal dynamics and  
949 adaptation to uncertain sea level rise: Optimal portfolios for salt marsh migration. *J. Environ.*  
950 *Econ. Manag.* 98, 102262. <https://doi.org/10.1016/j.jeem.2019.102262>

951 Wilson, C.A., Allison, M.A., 2008. An equilibrium profile model for retreating marsh shorelines in  
952 southeast Louisiana. *Estuar. Coast. Shelf Sci.* 80, 483–494.  
953 <https://doi.org/10.1016/j.ecss.2008.09.004>

954 Wilson, G.P., Lamb, A.L., Leng, M.J., Gonzalez, S., Huddart, D., 2005. Variability of organic  $\delta^{13}\text{C}$  and  
955 C/N in the Mersey Estuary, U.K. and its implications for sea-level reconstruction studies.  
956 *Estuar. Coast. Shelf Sci.* 64, 685–698. <https://doi.org/10.1016/j.ecss.2005.04.003>

957 Windham-Myers, L., Crooks, S., Troxler, T.G., 2019. *A Blue Carbon Primer: The State of Coastal*  
958 *Wetland carbon Science, Practice, and Policy*. Taylor & Francis Group, LLC, Boca Raton, FL  
959 33487-2742.

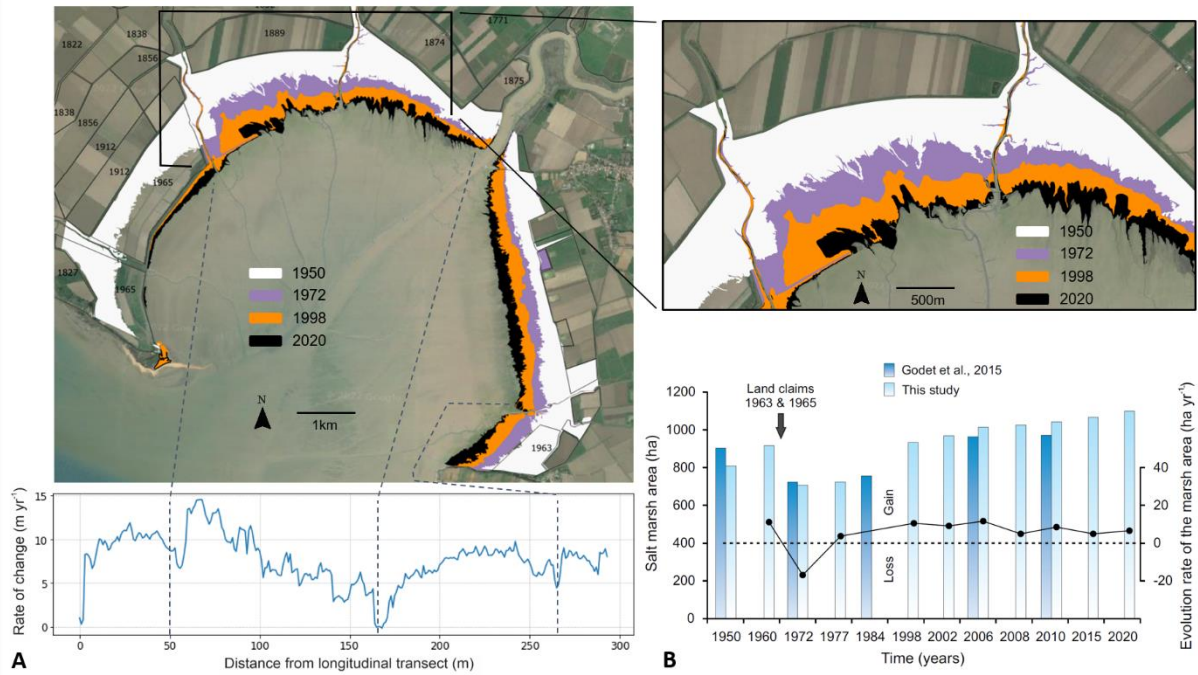
960 Yau, Y.Y., Xin, P., Chen, X., Zhan, L., Call, M., Conrad, S.R., Sanders, C.J., Li, L., Du, J., Santos, I.R.,  
961 2022. Alkalinity export to the ocean is a major carbon sequestration mechanism in a  
962 macrotidal saltmarsh 13.

963 Young, M.A., Macreadie, P.I., Duncan, C., Carnell, P.E., Nicholson, E., Serrano, O., Duarte, C.M., Shiell,  
964 G., Baldock, J., Ierodiaconou, D., 2018. Optimal soil carbon sampling designs to achieve cost-  
965 effectiveness: a case study in blue carbon ecosystems. *Biol. Lett.* 14, 20180416.  
966 <https://doi.org/10.1098/rsbl.2018.0416>

967 Zhang, X., Leonardi, N., Donatelli, C., Fagherazzi, S., 2019. Fate of cohesive sediments in a marsh-  
968 dominated estuary. *Adv. Water Resour.* 125, 32–40.  
969 <https://doi.org/10.1016/j.advwatres.2019.01.003>

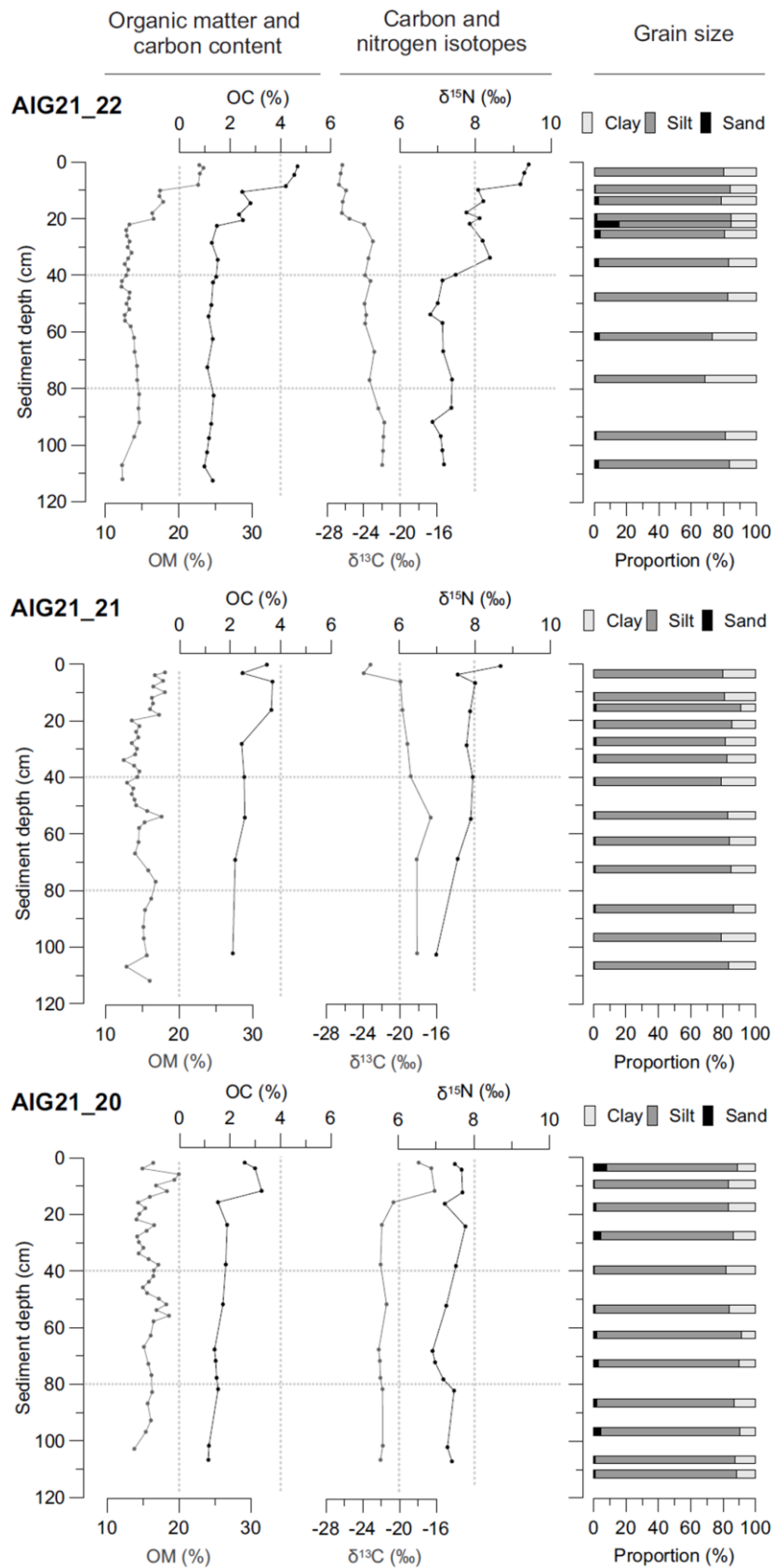
970





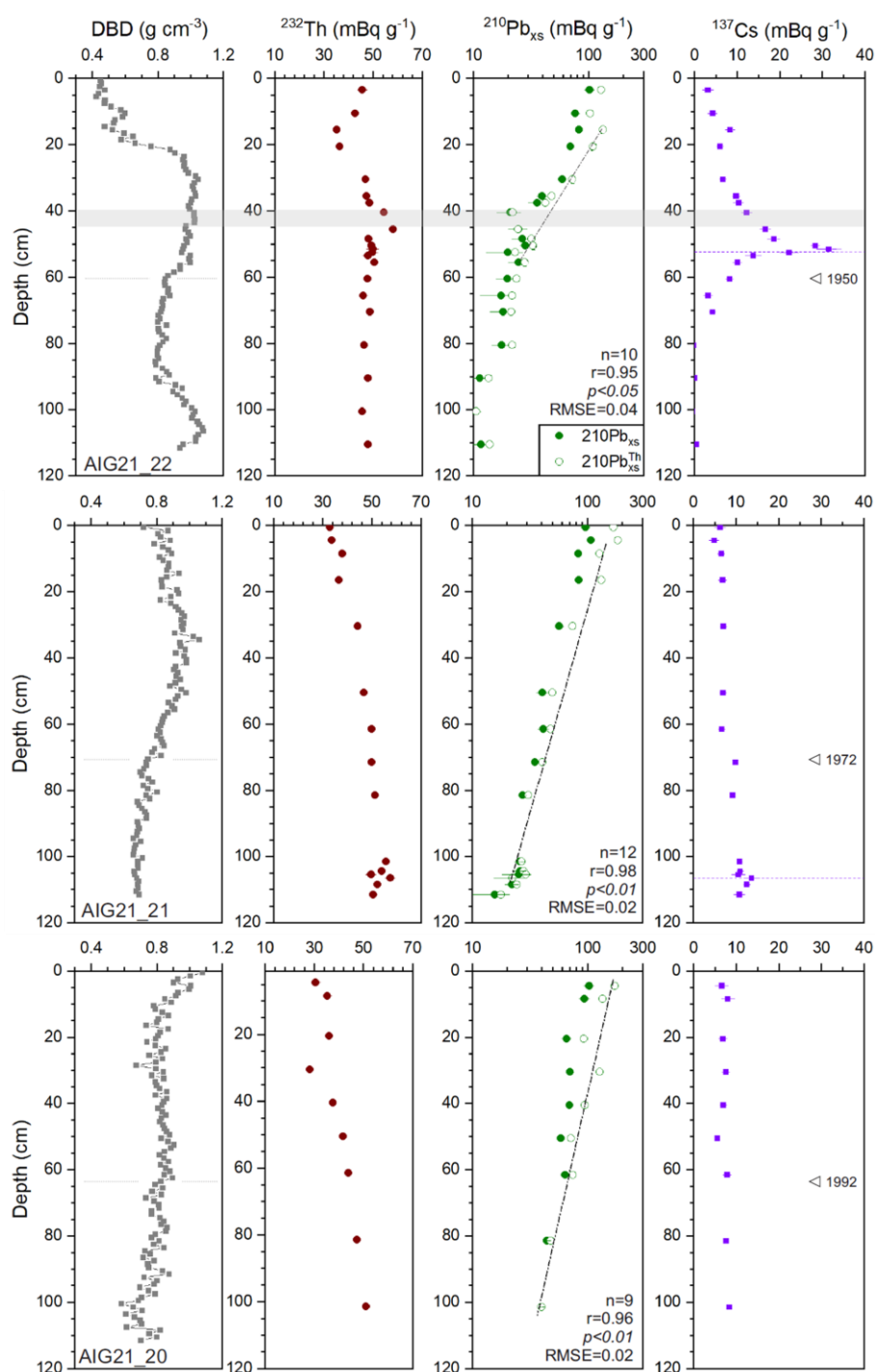
980  
981  
982  
983  
984  
985  
986

**Figure 2** Evolution of the saltmarsh boundary and area since 1950. **A** (*upper*) spatial progradation of the saltmarsh area, and (*lower left*) progradation rates (in m yr<sup>-1</sup>) calculated along a longitudinal transect for the period 1950-2020. **B** Temporal evolution of the saltmarsh area (in ha) and rates of change (in ha yr<sup>-1</sup>), for the whole bay. The vertical arrow marks the most recent land claims in 1963 and 1965, which induced an important reduction in the saltmarsh area. Data are from this study and Godet et al. (2015).



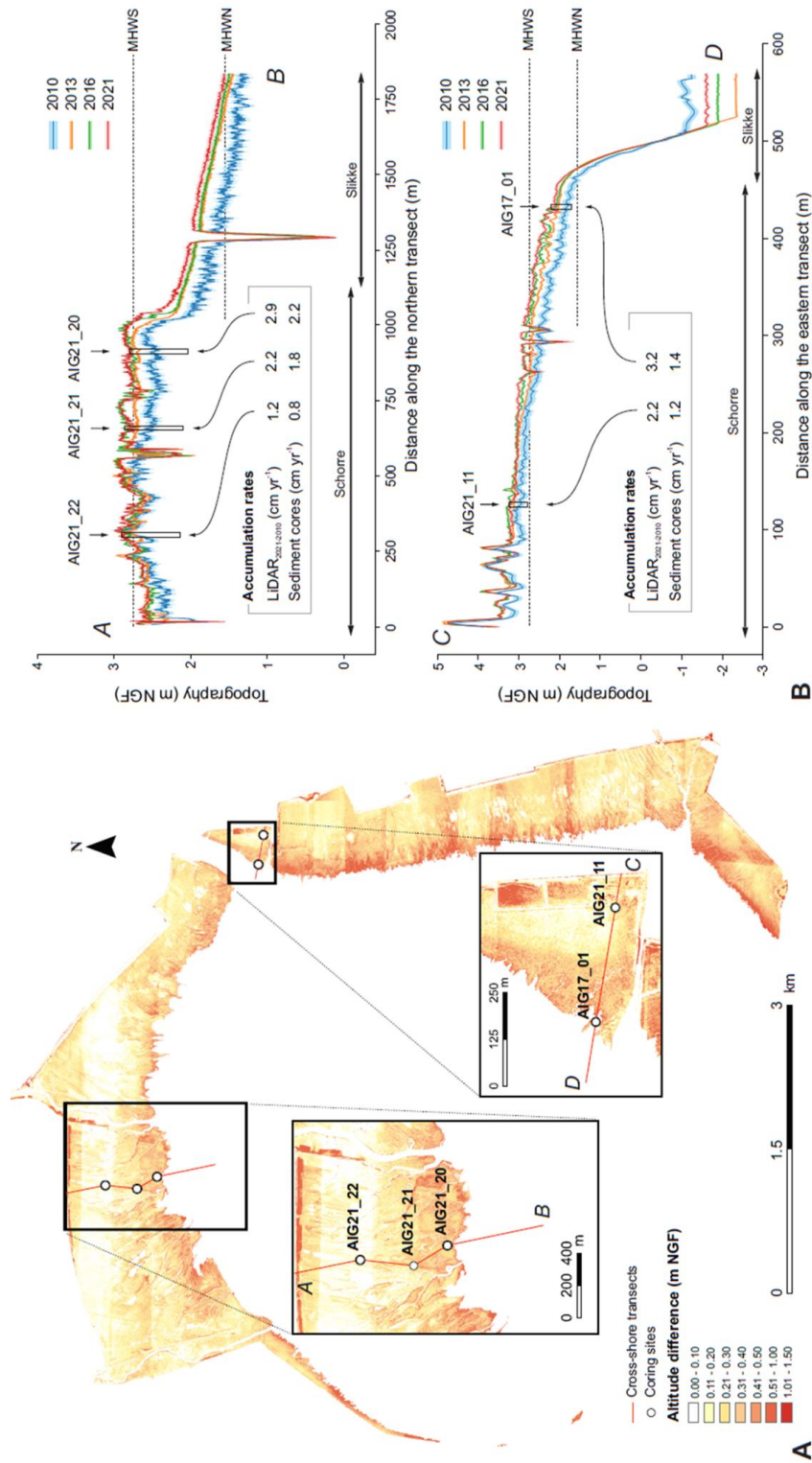
987

988 **Figure 3** Downcore profiles of OM and OC content, carbon and nitrogen isotopes, and grain size  
 989 fractions of the three cores of the northern transect. The grain-size distribution of each sediment  
 990 samples (*light gray*) and the average per core (*black*) are also presented.



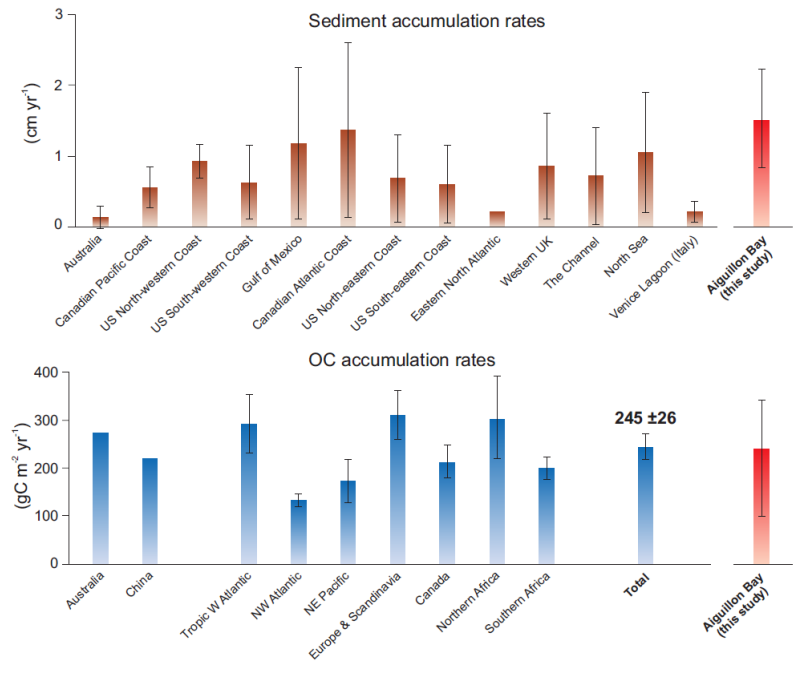
992

993 **Figure 4** Profiles with sediment depth of dry bulk density (DBD; gray), <sup>232</sup>Th (red), <sup>210</sup>Pb<sub>xs</sub> and <sup>210</sup>Pb<sub>xs</sub><sup>Th</sup>  
 994 (filled and empty green circles, respectively), and <sup>137</sup>Cs (purple) for the three cores of the northern  
 995 transect. The exponential regressions from the <sup>210</sup>Pb<sub>xs</sub><sup>Th</sup> profiles are used to calculate sediment and  
 996 mass accumulation rates. The gray horizontal rectangular in the AIG21\_22 profile highlights an  
 997 anomaly in <sup>210</sup>Pb<sub>xs</sub>. The corresponding layer thickness was subtracted to produce an event-free <sup>210</sup>Pb<sub>xs</sub><sup>Th</sup>  
 998 profile from which sediment accumulation rate was calculated. The dates on the y-axis correspond to  
 999 the saltmarsh boundary (reconstructed using aerial photographs and satellite images) on which the  
 1000 sediment core was retrieved. It marks the transition with depth between a tidal flat and a saltmarsh  
 1001 environment.



1002

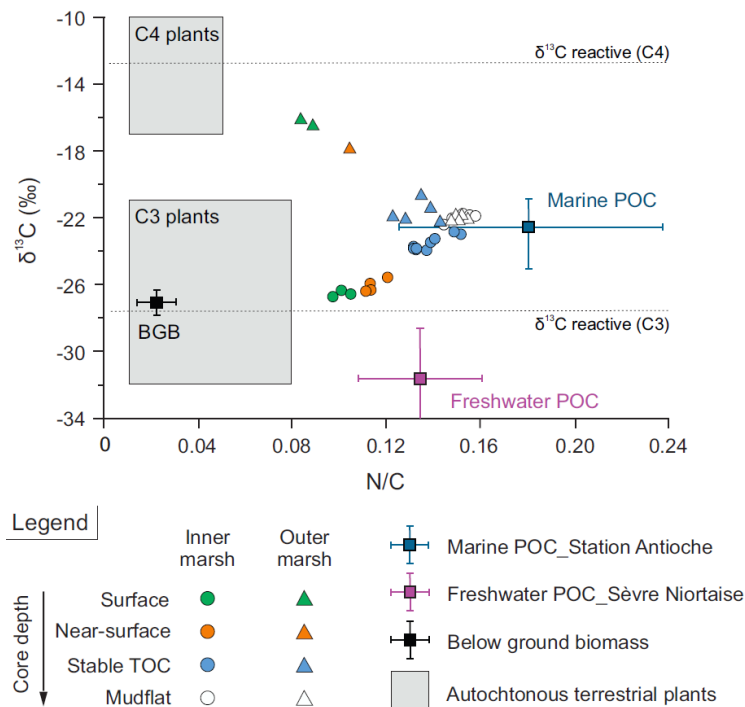
1003 **Figure 5** Mapping of the vertical evolution of the saltmarsh in the Aiguillon Bay using LiDAR data. **A**  
 1004 DEMs difference between 2021 and 2010 with the location of the coring transects. **B** Topographical  
 1005 changes along the two cross-shore transects for the four different years of LiDAR acquisition. Lower-  
 1006 elevation peaks in the profiles mark the presence of channels and/or creeks crossed by the transects.  
 1007 The coring sites are also reported on the topographical evolution of the transects, thus allowing a direct  
 1008 comparison with <sup>210</sup>Pb-based accumulation rates [note that LiDAR accumulation rates (cm yr<sup>-1</sup>) are  
 1009 calculated for the period 2010-2021; Table 2]. MHWs, and MHWN dashed lines represent the level of  
 1010 mean high water springs and mean high water neaps, respectively.



1011

1012 **Figure 6** Comparison between the Aiguillon Bay (red bars) and other saltmarsh studies: for sediment  
 1013 accumulation rates from temperate regions (upper panel), and OC accumulation rates from other  
 1014 regions worldwide (lower panel). This figure was built using review data from Giuliani and Bellucci  
 1015 (2019) for sediment accumulation rates, and from Ouyang and Lee (2014) for OC accumulation rates.

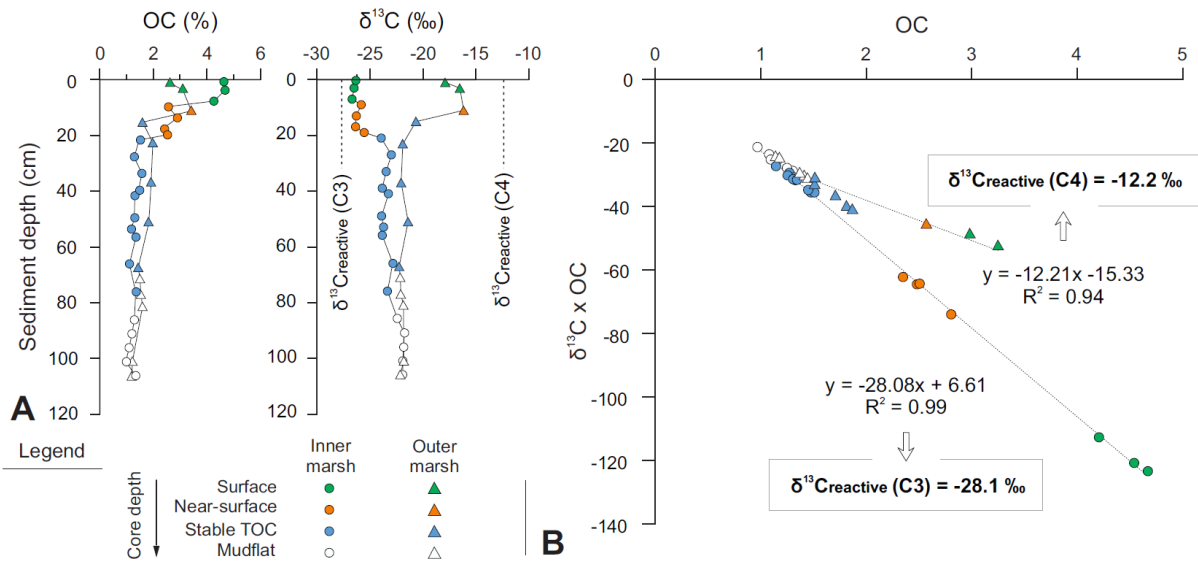




1016

1017 **Figure 7** Comparison of  $\delta^{13}\text{C}$  and N/C signatures of the Aiguillon saltmarsh sediments to OM sources.  
 1018 The use of the N/C ratio instead of C/N allows better separating the OM sources, graphically. Sediments  
 1019 are classified according to the position of the core on the saltmarsh: inner (*circles*) and outer  
 1020 (*triangles*), and to the depth in the core. The potential OM sources considered are: (i) freshwater POC  
 1021 from upstream the Sèvre Niortaise, in Marans (*purple square with error bars*; Richard, 2000); (ii) marine  
 1022 POC in the Pertuis d'Antioche (*blue square with error bars*; SOMLIT data); and (iii) C3- and C4-based  
 1023 autochthonous OM from saltmarsh (Lamb et al., 2006 and references therein). The signature of below-  
 1024 ground biomass from the inner marsh is also reported (BGB, *black square with error bars*; this study).  
 1025 Horizontal dashed lines refer to the isotopic signature of reactive sedimentary OC dominated by C3  
 1026 and C4 plants (*cf. Fig. 8b*).

1027



1028

1029 **Figure 8** Elementary and isotopic signatures of saltmarsh sediments for the landward site (*circles*) and  
1030 the seaward site (*triangles*), colored according to sediment depth. **A** Depth-profiles of OC and  $\delta^{13}\text{C}$ .  
1031 Mudflat and marsh samples characterized by stable OC differ significantly from surface and near-  
1032 surface samples by their OC content and  $\delta^{13}\text{C}$  signature. **B**  $\delta^{13}\text{C} \times \text{OC}$  against OC used to determine the  
1033 signature of reactive OC as proposed by Komada et al. (2022). The slopes derived from cores of the  
1034 inner and outer marsh suggest a  $\delta^{13}\text{C}_{\text{reactive}}$  of -12.2 ‰ and -28.1 ‰ for sediments influenced by C4  
1035 and C3 vegetation, respectively.

1036 **Table 1** Data compilation by site for the saltmarshes of the Aiguillon Bay, with sediment accumulation  
 1037 rates (SAR in  $\text{cm yr}^{-1}$ ), mass accumulation rates (MAR, in  $\text{g m}^{-2} \text{yr}^{-1}$ ), OC content (in %), and OC  
 1038 accumulation rates (CAR, in  $\text{g m}^{-2} \text{yr}^{-1}$ ). The error bound to sedimentation rates refers to the  
 1039 propagation of the error on the slope the  $^{210}\text{Pb}$  exponential regressions. \* Cores were too short to  
 1040 observe the  $^{137}\text{Cs}$  peak; \*\* SAR and MAR are based on  $^{210}\text{Pb}_{\text{xs}}$ , without Th standardizing.

1041

Site	Core coordinates		$^{137}\text{Cs}$ peak position		SAR		MAR		OC	
			depth (cm)	cumulative-mass ( $\text{g cm}^{-2}$ )	based on $^{137}\text{Cs}$	based on $^{210}\text{Pb}_{\text{xs}}$ Th	based on $^{137}\text{Cs}$	based on $^{210}\text{Pb}_{\text{xs}}$ Th	content (%)	CAR ( $\text{gC m}^{-2} \text{yr}^{-1}$ )
					( $\text{cm yr}^{-1}$ )	( $\text{cm yr}^{-1}$ )	( $\text{g cm}^{-2} \text{yr}^{-1}$ )	( $\text{g cm}^{-2} \text{yr}^{-1}$ )		
Latitude	Longitude									
Northern transect										
<b>AIG21_20</b>	46.311111	-1.17439	> 112 *	> 90.5*	> 1.91*	<b>2.22 ± 0.32</b>	> 1.55*	1.83 ± 0.30	1.86 ± 0.16	<b>340 ± 29</b>
<b>AIG21_21</b>	46.31292	-1.17615	106.5	88.3	1.82	<b>1.85 ± 0.09</b>	1.51	1.50 ± 0.07	2.49 ± 0.03	<b>373 ± 5</b>
<b>AIG21_22</b>	46.31591	-1.17592	51	41.8	0.87	<b>0.84 ± 0.06</b>	0.71	0.74 ± 0.05	1.44 ± 0.15	<b>107 ± 11</b>
Eastern transect										
<b>AIG17_01</b>	46.303183	-1.13131				<b>1.41 ± 0.19</b>		1.24 ± 0.20 **		
<b>AIG21_11</b>	46.30252	-1.12912	> 36 *	> 25.2 *	> 0.61 *	<b>1.24 ± 0.26</b>	> 0.43*	0.86 ± 0.12	2.12 ± 0.56	<b>182 ± 48</b>

1042

1043

1044

1045 **Table 2** Evolution through time of the sediment volume gain (in  $\text{m}^3$ ) and sediment accumulation rates  
 1046 (in  $\text{cm yr}^{-1}$ ) in saltmarshes of the whole bay inferred using LiDAR data. Values are calculated for the  
 1047 entire instrumental period (2010 to 2021) and more recent periods (2013 to 2021, and 2016 to 2021).

	2010 – 2021 (entire instrumental period)	2013 – 2021	2016 – 2021
Sediment volume gain ( $\text{m}^3$ )	1 419 043 ± 458 732	426 251 ± 213 116	216 426 ± 267 440
Salt marsh area in 2021 ( $\text{m}^2$ )	11 000 200 ± 1 200	11 000 200 ± 1 200	11 000 000 ± 1 200
Sediment accumulation rate ( $\text{cm yr}^{-1}$ )	1.17 ± 0.38	0.48 ± 0.24	0.39 ± 0.49

1048